澳門科技大學

MACAU UNIVERSITY OF SCIENCE AND TECHNOLOGY

双有源桥式DC-DC变换器的暂态调控技术

Transient Modulation and Control Techniques for Dual-Active-Bridge (DAB) DC-DC Converters

孙川

澳门科技大学

csun@must.edu.mo

https://chuansun-pe.github.io/

2026年4月13日

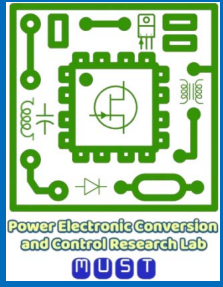

Dedication to practical studies,
Enhancement of knowledge, Ability and Quality.

意誠格物

Contents

- ▶ Introduction
- ▶ Overview of Existing Modulation and Control Strategies
- ▶ Optimized Transient Phase-Shift Modulation for NR-DABC
- ▶ Optimized Transient Phase-Shift Modulation for SR-DABC
- ▶ Conclusions

On the Necessity of Improving IBDC's Dynamics

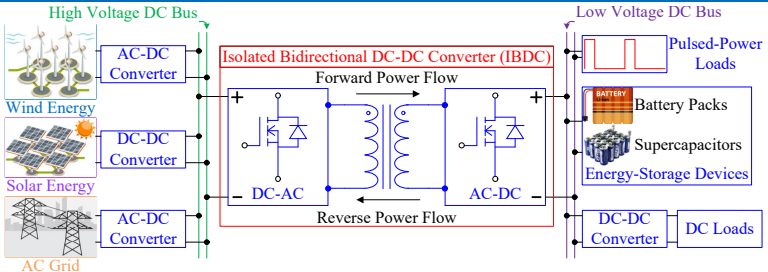

Figure 1: Distributed renewable energy generation and storage system.

Why Does IBDC Require Fast Dynamics?

- Large uncertain and unpredictable power flow fluctuations induced by renewable energy sources.
- IBDCs are increasingly used in applications (e.g., pulsed-power loads) requiring fast responses.
- Fast responses allow the use of smaller output capacitors, thereby reducing the filter size.
- Existing control methods have shown their inability to achieve fast and smooth load transitions.

⇒ Further optimization of the dynamics and control design is always necessary!

Typical Topologies of DABC

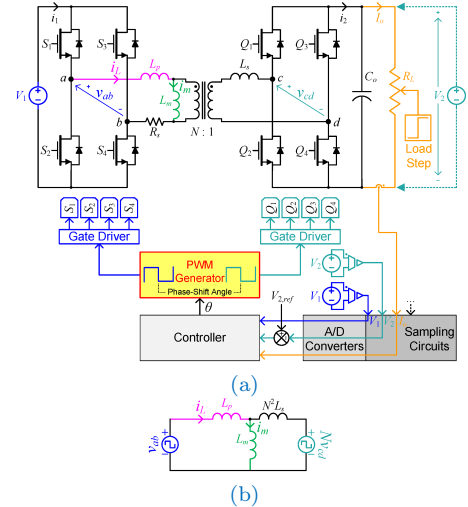

Figure 2: Circuit schematic of NR-DABC.

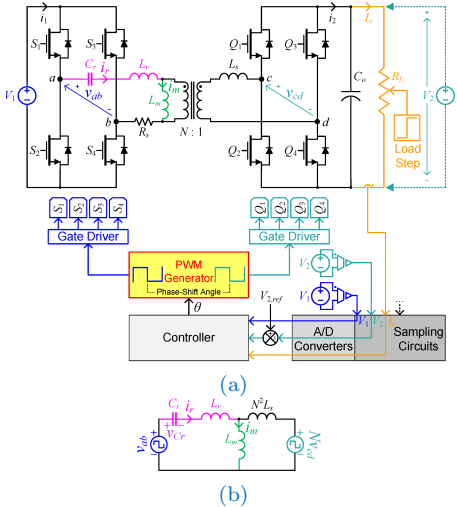

Figure 3: Circuit schematic of SR-DABC.

Benefits

simple structure,
galvanic isolation,
high efficiency,
high power density,
flexibility of control,
ease of modulation,
wide ZVS range, etc.

Basic Principles

controlling the shape of the high-frequency-link current is equivalent to controlling the direction and amount of the power flow between the two sides.

Roles of Controller and Transient Modulation

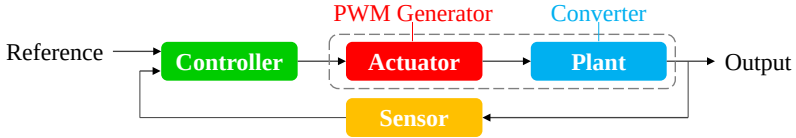

Figure 4: Relationship between actuator and controller.

In response to a load change (power adjustment), the current value of the control variable (i.e., $\theta[n]$) should be changed to the desired value (i.e., $\theta[n+1]=\theta[n]+\Delta\theta$).

Differences Between Control Design and Transient Modulation

- The controller determines the optimal control variables (i.e., phase-shift angles) to maintain a constant output voltage, according to the feedback information.
- The PWM generator (actuator) determines the switching sequences for driving power switches. (**It is the responsibility of PWM generator to specify the way to update the control variables.**)

⚠ **As a result, both the controller and transient modulation determined by PWM generator can affect the dynamic performance of a closed-loop controlled DABC.**

Transient DC Offsets in NR-DABC

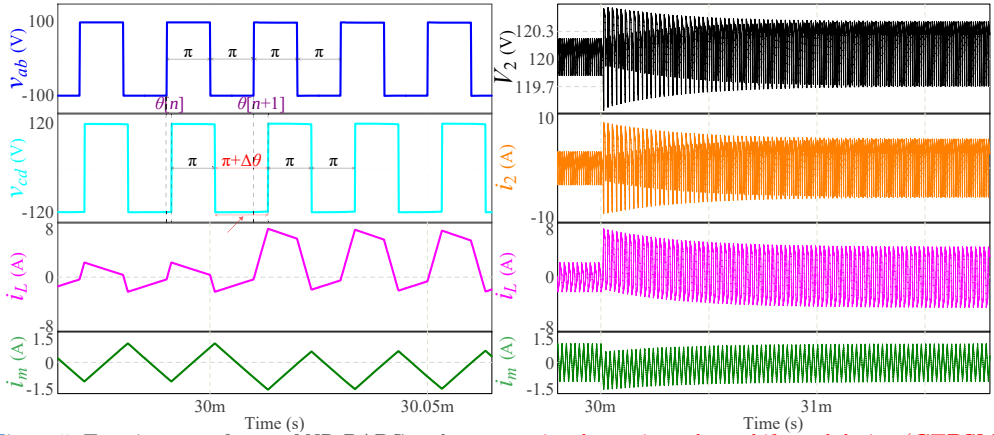

Figure 5: Transient waveforms of NR-DABC under conventional transient phase-shift modulation (**CTPSM**).

☹ Risk of saturation in magnetic elements, triggering of protection, long settling time, etc.

Transient Beat-Frequency Oscillations in SR-DABC

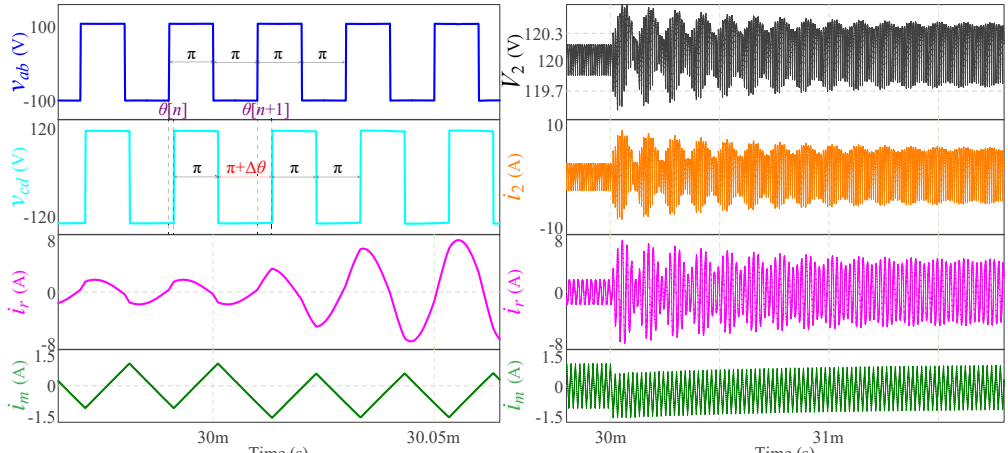

Figure 6: Transient waveforms of SR-DABC under CTPSM.

☹ High voltage and current stresses, power device ageing and damage, long settling time, etc.

Motivation and Objectives

Benefits of Using Fast and High-Gain Controller

Reduced Response Time, Lower Output Voltage Fluctuation, Smaller Steady-State Tracking Error, More Compact System Integration, etc.

Potential Problems Posed by CTPSM

A fast and high-gain controller can lead to abrupt and large variations in the control variables, thus producing severe transient dc offsets and oscillations under CTPSM.

Motivation and Objectives ★ **How to ensure a fast but smooth transition process?**

⇒ **The high-frequency-link current of DABC should be modulated and controlled properly!**

⇒ This motivates our research to (1) gain a thorough understanding of DABC's transient behaviour, and (2) develop **Optimized Transient Phase-Shift Modulation (OTPSM) + Fast Controller** for achieving ultra-fast, dc-offset-free, and oscillation-free dynamics.

Contents

- Introduction
- Overview of Existing Modulation and Control Strategies
- Optimized Transient Phase-Shift Modulation for NR-DABC
- Optimized Transient Phase-Shift Modulation for SR-DABC
- Conclusions

Optimized Steady-State Modulation Strategies

for Improving Conversion Efficiency

Outer Phase-shift Angle: θ_2
Inner Phase-shift Angles: θ_1 and θ_3
SPS Modulation: $\theta_2 \neq 0$, $\theta_1 = 0$, and $\theta_3 = 0$
DPS Modulation: $\theta_2 \neq 0$, $\theta_1 = 0$, or $\theta_3 = 0$
TPS Modulation: $\theta_2 \neq 0$, $\theta_1 \neq 0$, and $\theta_3 \neq 0$

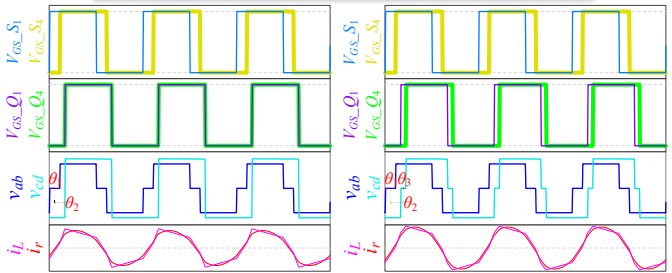

Figure 7: Typical steady-state waveforms of NR-DABC and SR-DABC under (a) DPS and (b) TPS modulation schemes.

Steady-State Efficiency Optimization

Optimization Problem: for a given power level, different combinations of θ_1, θ_2, and θ_3 can be found under multi-phase-shift (MPS) modulation schemes for maximizing the overall efficiency.

Optimization Objectives: minimum root-mean-square (RMS) or peak-to-peak value for DABC's high-frequency-link current, low or zero backflow power, wide-range ZVS operation, etc.

Optimization Methods: Lagrange multipliers and Karush–Kuhn–Tucker (KKT) conditions, particle swarm optimization (PSO) algorithm, genetic algorithm (GA), artificial intelligence (AI) algorithm, etc.

Optimized Transient Modulation Strategies (OTPSM)

for Eliminating Transient DC Offsets in NR-DABC

Cause of Transient DC Offsets

Any asymmetry in the inductor volt-second product will lead to magnetic flux imbalance that induces dc offsets, and hence the directly-adjusted transient switching pattern under CTPSM will lead to a monotonic increase in the volt-second product or flux linkage of the inductor during transient state.

Basic Principle of OTPSM

To design specific switching sequences that can seamlessly modify the inductor current and achieve dynamic volt-second balance during transient state.

Main Advantage of OTPSM

To directly update a large-amplitude phase-shift increment or decrement within about one switching cycle and to limit the inductor current.

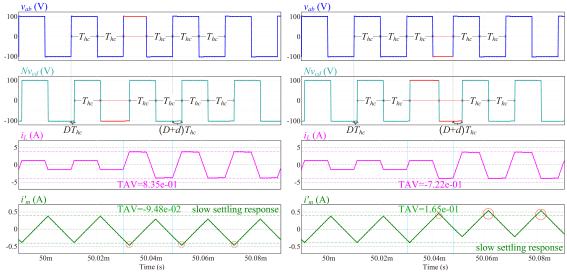

(a) (b)

Both Type-A and Type-B OTPSM strategies originate from the principle of **relative motion**.

Drawbacks: (1) serious transient dc offset and long settling time exist in i_m; (2) designed transient pulse widths under Type-A and Type-B OTPSM strategies are related to the voltage gain $M = NV_2/V_1$.

Optimized Transient Modulation Strategies (OTPSM)

for Eliminating Transient DC Offsets in NR-DABC

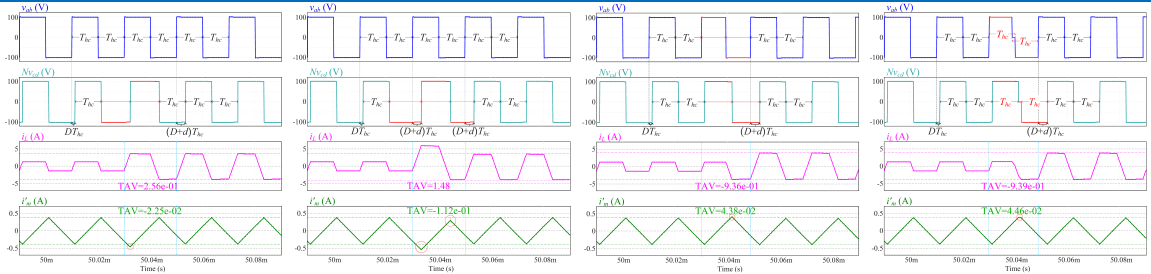

Figure 8: Simulated open-loop transient response of NR-DABC under different types of OTPSM strategies: (a) Type A. (b) Type B. (c) Type C. (d) Type D. (e) Type E. (f) Type F.

Type-C and Type-E OTPSM strategies generate two equal-width transient pulses by consecutively moving two edges of v_{ab} and/or v_{cd}, while Type-D OTPSM continuously generates three unequal-width transient pulses in v_{cd}. Type-F OTPSM introduces zero-voltage durations into v_{ab} and/or v_{cd}.

Drawbacks: All Type-C to Type-F OTPSM strategies can lead to overshoots/undershoots in i_m, and the average values of both i_L and i_m during transient state are still not zero.

Disadvantages of Different Control Methods

Pure PI Control

The interaction between the two tuning parameters makes it challenging to simultaneously achieve fast and stable performance over the whole operating range.

Pre-Calculated Feed-Forward Control

A lookup table is used to decouple the complex relationship between phase-shift angle and load current, but the control performance relies on the difference between actual and nominal circuit parameters.

Virtual Direct Power Control

It is effective in cancelling the effects of circuit parameters, but its performance degrades at light-load conditions.

Current-Mode Control
Natural-Switching-Surface Control
Deadbeat Current Control

They are not desirable solutions because the high-frequency-link current of DABC must be sampled by costly high-bandwidth sensors at a high sampling rate (i.e., at least twice the switching frequency).

Disturbance-Observer Control
Sliding-Mode Control
Model Predictive Control (MPC)

In exchange for fast transient response, the controller's gain and bandwidth must be increased. The control variables (i.e., phase-shift angles) will undergo large-magnitude changes under CTPSM, thus resulting in large transient dc offsets and oscillations.

How to Achieve Optimal Dynamic Performance?

☹ Significant Limitations of Existing OTPSM Schemes

1. The inner links between different OTPSM schemes are unclear. Existing OTPSM strategies developed for NR-DABC cannot achieve complete transient dc-offset elimination, and there is no easy-to-implement OTPSM for SR-DABC.
2. Most previous OTPSM strategies have only been validated in open-loop conditions, and hence their OTPSM algorithms (transient pulse widths) must be pre-calculated.
3. A much-debated question is whether such OTPSM strategies can truly bring about positive effects on improving the dynamics of closed-loop controlled DABC.
   A pure PI controller often suffers from a trade-off between response time and stability margin. If a PI controller's gain is too high, the system may become unstable.

New Solution: Sensorless OTPSM+Fast Controller (e.g., MPC)

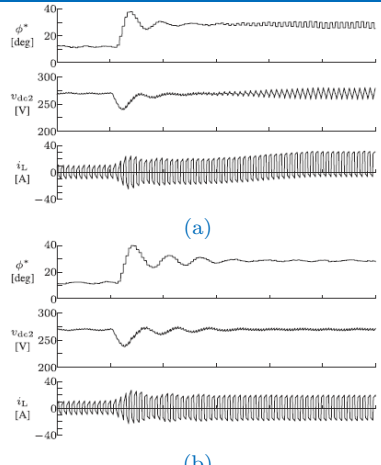

Figure 9: Dynamics of NR-DABC under a high-gain PI controller with (a) CTPSM and (b) Type-F OTPSM. (Ref.: TPEL.2017.2773267)

Contents

- Introduction
- Overview of Existing Modulation and Control Strategies
- Optimized Transient Phase-Shift Modulation for NR-DABC
- Optimized Transient Phase-Shift Modulation for SR-DABC
- Conclusions

Primary-Referred Equivalent Circuits of NR-DABC

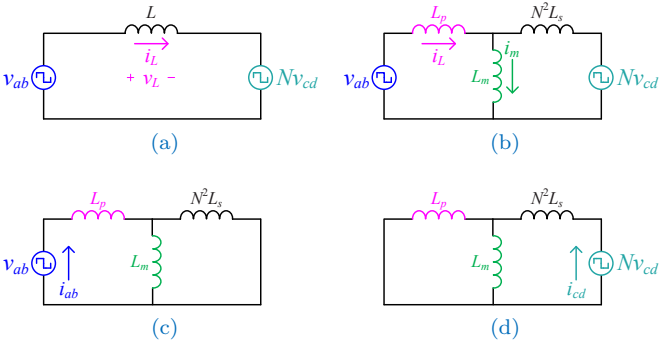

Figure 10: Primary-referred equivalent circuits of NR-DABC. (a) Ideal equivalent circuit. **(b) T-model equivalent circuit**. Applying superposition principle. (c) Individual contribution due to v_{ab}. (d) Individual contribution due to Nv_{cd}.

Magnetizing Inductance: $L_m \gg L$

Total Equivalent Series Inductance: $L = L_p + N^2 L_s$

Applying Superposition Principle

$$i_L = i_{ab} - \frac{L_m}{L_m + L_p} i_{cd} \approx i_{ab} - i_{cd} \quad (1)$$

$$i_m = \frac{N^2 L_s}{L_m + N^2 L_s} i_{ab} + \frac{L_p}{L_m + L_p} i_{cd} \quad (2)$$

Steady-State Power Transfer Model

$$P = \frac{1}{2T_{hc}} \int_0^{2T_{hc}} v_{ab}(t) i_L(t) \mathrm{d}t \approx \frac{N V_1 V_2 T_{hc} D(1-D)}{L} \quad (3)$$

During Transient State

D —needs to be adjusted to→ $D + d$

Unified Transient-Modulation Framework for NR-DABC

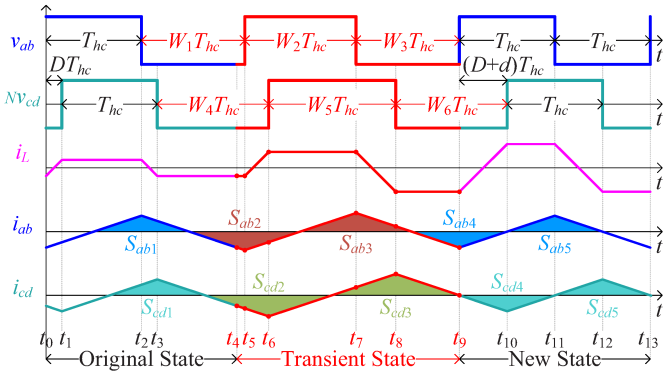

Figure 11: Unified framework of OTPSM strategies for NR-DABC.

- Constraint ①: The time interval $t_{10}-t_9$ should be equal to $(D+d)T_{hc}$. $\Rightarrow W_1+W_2+W_3+d=W_4+W_5+W_6$
- Constraint ②: $i_L(t_9)=i_L(t_{13})$. $\Rightarrow$ $0=(2-2W_1+2W_2-2W_3)+(2W_1+2W_2+2W_3-4W_5-2+2d)M$

General Solution of OTPSM

All the Type-A to Type-E OTPSM strategies fulfill the two constraints.

☹ $W_1 \sim W_6$ cannot be decoupled from M.

☺ Eliminating the dependence of M yields a general solution for sensorless OTPSM:

$$\begin{cases} 1+W_2=W_1+W_3 \\ 1+W_5=W_4+W_6 \\ 2W_2+d=2W_5. \end{cases} \tag{4}$$

Minimizing Transient DC Offsets

☺ The average values of i_{ab} and i_{cd} are zero (symmetric about the horizontal axis).

$$\begin{cases} W_1=W_3=(1+W_2)/2 \\ W_4=W_6=(1+W_5)/2 \\ 2W_2+d=2W_5 \end{cases} \tag{5}$$

Two Simple Particular Solutions of (5) ⇒ SS-OTPSM

☺ Type-I SS-OTPSM (v_{cd} *is unmodulated*):

$$\begin{cases} W_1 = W_3 = 1 - \frac{d}{4} \\ W_2 = 1 - \frac{d}{2} \\ W_4 = W_5 = W_6 = 1 \end{cases} \tag{6}$$

☺ Type-II SS-OTPSM (v_{ab} *is unmodulated*):

$$\begin{cases} W_1 = W_2 = W_3 = 1 \\ W_4 = W_6 = 1 + \frac{d}{4} \\ W_5 = 1 + \frac{d}{2} \end{cases} \tag{7}$$

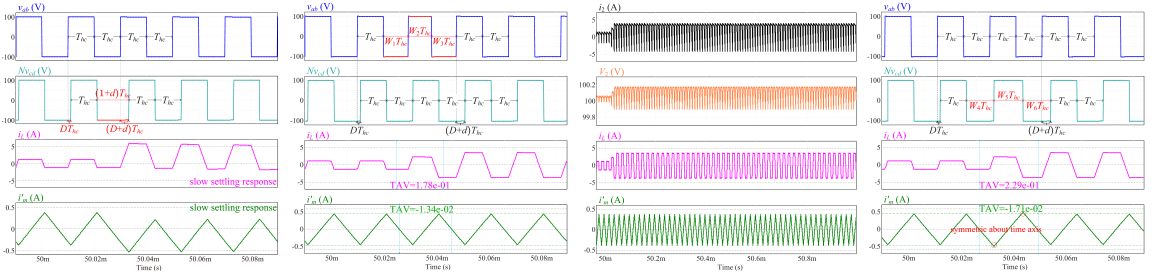

Figure 12: Simulated open-loop transient response for an increase in the phase-shift ratio under CTPSM and SS-OTPSM strategies. (a) Transient waveforms under CTPSM. (b) Transient waveforms under Type-I SS-OTPSM. (c) Zoomed-out transient waveforms of i_2, V_2, i_L, and i_m under Type-I SS-OTPSM. (d) Transient waveforms under Type-II SS-OTPSM.

Parameter Sensitivity Analysis for Type-I SS-OTPSM

☺ SS-OTPSM (6) is always effective to eliminate transient dc offsets under different circuit parameters.

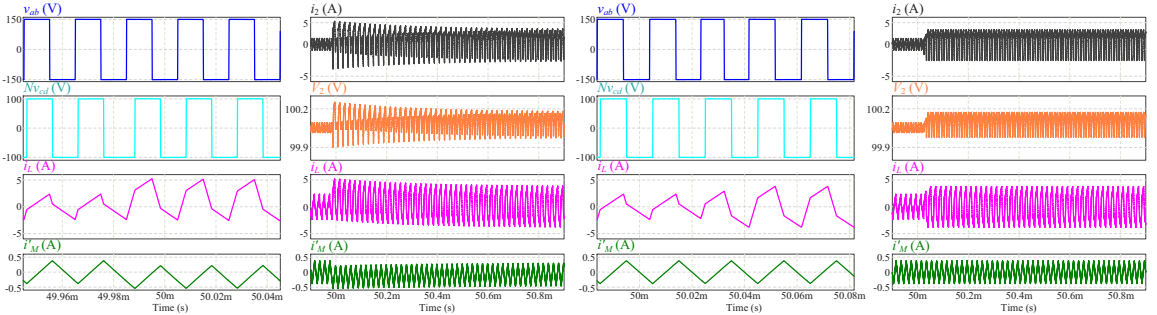

Figure 13: Parameter sensitivity analysis for Type-I SS-OTPSM. Simulated open-loop transient response under (a) CTPSM and (b) Type-I SS-OTPSM. The simulation parameters are as follows: $f_s = 50$ kHz, $V_1 = 150$ V, $V_2 = 100$ V, $L_p = 150$ μH, $L_s = 1.70$ μH, $L_m = 650$ μH, and the phase-shift ratio is changed from $\frac{1}{9}$ to $\frac{1}{3}$.

Performance of SS-OTPSM

Table 1: Main Features of Different OTSPSM Strategies for NR-DABC.

Type	DOF	W1	W2	W3	W4	W5	W6	Sensorless	Complexity*	CE†
CTPSM	1	1	1	1	$1+d$	1	1	Yes	$\star$	No
A OTPSM	2	1	$1-\frac{dM}{M+1}$	1	$1+\frac{d}{M+1}$	1	1	No	$\star\star\star$	No
B OTPSM	3	1	1	$1-d$	1	$1+\frac{d}{2M}$	$1-\frac{d}{2M}$	No	$\star\star\star\star$	No
C OTPSM	2	1	1	1	$1+\frac{d}{2}$	$1+\frac{d}{2}$	1	Yes	$\star\star$	IE‡
D OTPSM	3	1	1	1	$1+d$	$1+\frac{d}{2}$	$1-\frac{d}{2}$	Yes	$\star\star\star$	IE‡
E OTPSM	4	1	$1-\frac{d}{4}$	$1-\frac{d}{4}$	1	$1+\frac{d}{4}$	$1+\frac{d}{4}$	Yes	$\star\star\star$	IE‡
F OTPSM	6	—	—	—	—	—	—	Yes	$\star\star\star\star\star$	IE‡
I SS-OTPSM	3	$1-\frac{d}{4}$	$1-\frac{d}{2}$	$1-\frac{d}{4}$	1	1	1	Yes	$\star$	Yes
II SS-OTPSM	3	1	1	1	$1+\frac{d}{4}$	$1+\frac{d}{2}$	$1+\frac{d}{4}$	Yes	$\star$	Yes

§ Expressions in the first row satisfy $D>0$, $d<0$ and $D+d<0$, while expressions in the second row satisfy $D<0$, $d>0$ and $D+d>0$.
$\star$ Low $\star$, Moderate $\star\star$, High $\star\star\star$, Very High $\star\star\star\star$, Extreme $\star\star\star\star\star$.
† Complete elimination (CE) of transient dc offsets in both i_L and i_M. ‡ Incomplete elimination (IE).

It can be verified that all types of OTPSM strategies except Type-*F* OTPSM can be formulated by constraints ① and ②, while Type-*C* to Type-*E* OTPSM and SS-OTPSM strategies can also be formulated by (4). The expressions for the SS-OTPSM strategies, i.e., (6), and (7), can be regarded as the optimum solutions of (4).

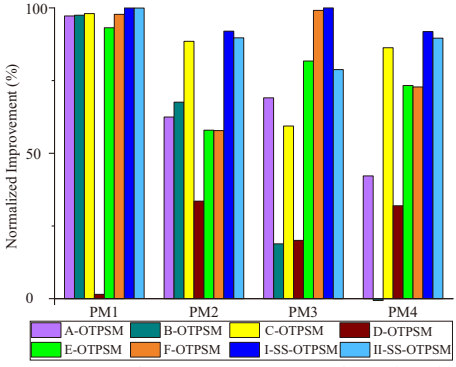

Figure 14: Performance evaluation of the OTPSM strategies in open-loop simulations.

PM1: maximum overshoot of the peak amplitude of i_L.
PM2: absolute value of the transient dc offset of i_L.
PM3: maximum overshoot of the peak amplitude of i_m'.
PM4: absolute value of the transient dc offset of i_m'.

Cycle-by-Cycle Implementation of SS-OTPSM

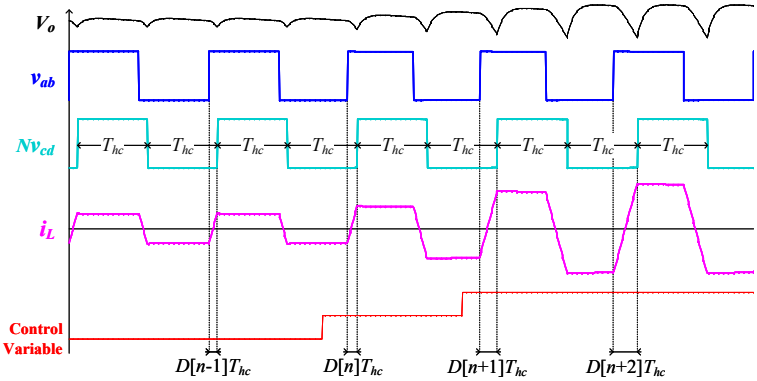

Figure 15: Cycle-by-Cycle Implementation of SS-OTPSM.

☺ It is able to dynamically update the control variable D by using SS-OTPSM in a cycle-by-cycle manner, thus achieving dc-offset-free dynamics.

Common Closed-Loop Controllers for DABCs

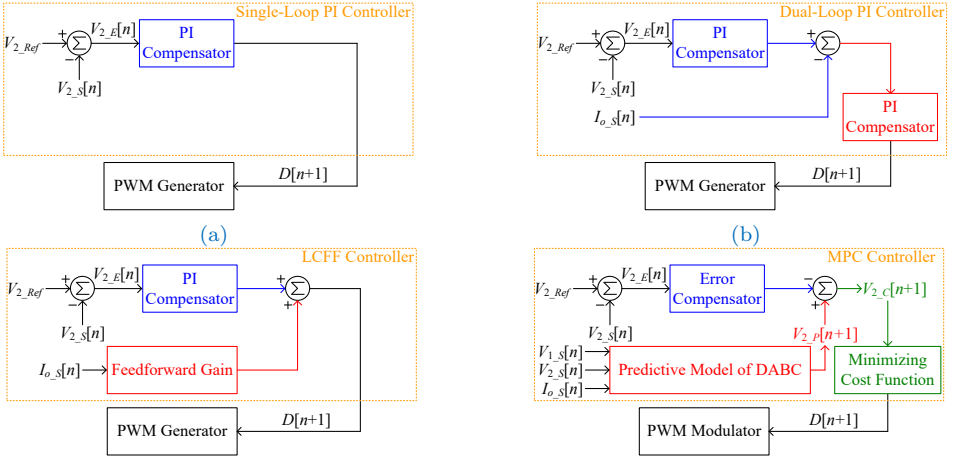

Figure 16: Different closed-loop controllers for DAB converters. (a) Single-Voltage-Loop PI Controller, (b) Dual-Loop PI (DLPI) Controller, (c) Load-Current Feed-Forward (LCFF) Controller, and (d) MPC.

Closed-Loop Simulation Results Under DLPI Controller

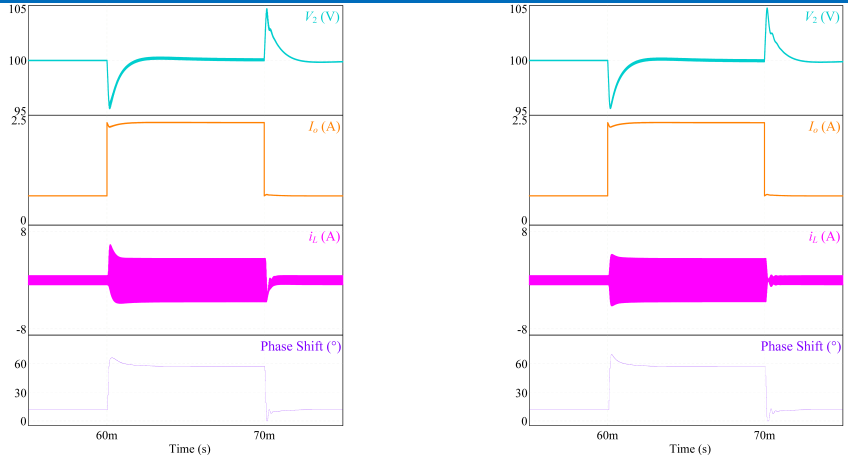

Figure 17: Simulated dynamics under dual-loop PI (DLPI) controller with (a) CTPSM and (b) SS-OTPSM.

Closed-Loop Simulation Results Under LCFF Controller

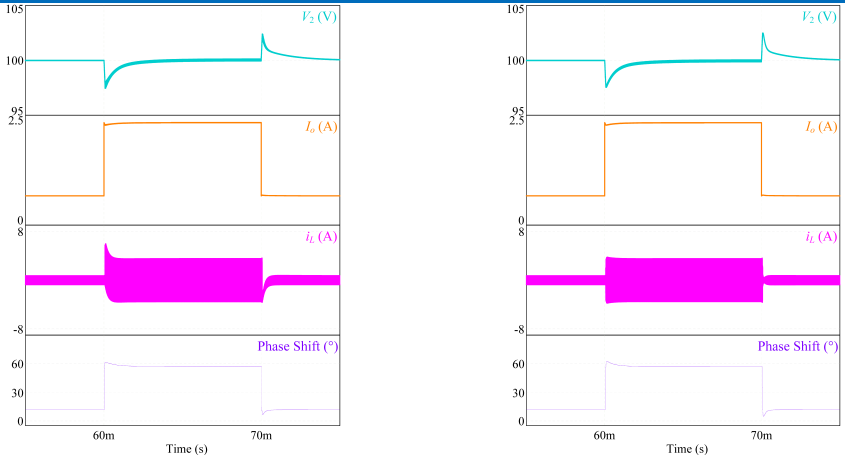

Figure 18: Simulated dynamics under load-current feed-forward (LCFF) controller with (a) CTPSM and (b) SS-OTPSM.

☺ **SS-OTPSM is inherently compatible with most controllers.**

Conventional MPC Design

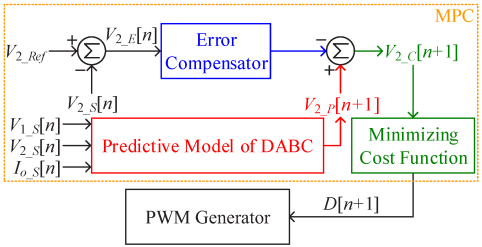

Figure 19: Conceptual block diagram of MPC.

Although different MPCs have been developed for NR-DABC, they are generally described by Fig. 19. The major differences between the existing MPC schemes lie in the predictive model, error compensator and cost function.

A simple MPC scheme = one-step prediction + PI compensator + quadratic cost function.

Conventional MPC

① The dynamic behavior of V_2 is described by

$$C_o\frac{\mathrm{d}V_2}{\mathrm{d}t}=\bar{i}_2-I_o=\frac{P}{V_2}-I_o=\frac{NV_1T_{hc}D(1-D)}{L}-I_o \tag{8}$$

② Discretizing (8) using forward Euler approximation,

$$V_{2\_P}[n+1]\approx V_{2\_S}[n]+2T_{hc}V_2{}'[n] \tag{9}$$

③ The cost function J is defined as

$$J=[V_{2\_Ref}-V_{2\_C}[n+1]]^2 \tag{10}$$

④ Minimizing J yields the optimal phase-shift ratio,

$$D[n+1]=\frac{1}{2}\left(1-\sqrt{1-\frac{4K_2}{K_1}}\right) \tag{11}$$

$$K_1=\frac{2NT_{hc}^2V_{1\_S}[n]}{LC_o} \tag{12}$$

$$\begin{aligned}K_2=&2T_{hc}I_{o\_S}[n]/C_o+V_{2\_E}[n]+(K_pV_{2\_E}[n]+K_i\sum_{\tau=0}^{n}V_{2\_E}[\tau])\\=&2T_{hc}I_{o\_S}[n]/C_o+(K_p^*V_{2\_E}[n]+K_i\sum_{\tau=0}^{n}V_{2\_E}[\tau])\end{aligned} \tag{13}$$

$$K_p^*=K_p+1 \tag{14}$$

Enhanced MPC (EMPC) Design

How to make an MPC faster?

A major problem with conventional predictive model is that the output/transmission power P (3) is derived based on steady-state waveforms; hence it cannot accurately predict the average power transferred during transient state.

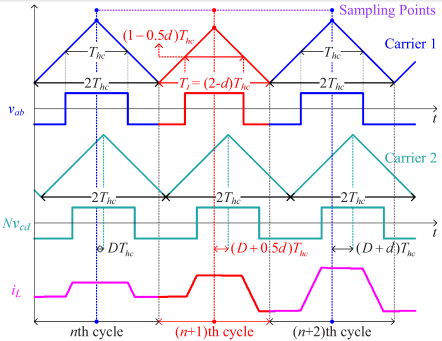

Figure 20: Implementation of Type-I SS-OTPSM.

EMPC for SS-OTPSM

Average power under SS-OTPSM over the $(n+1)^{th}$ cycle is given by,

$$P^* = \frac{1}{(2-d)T_{hc}} \int_0^{(2-d)T_{hc}} v_{ab}(t) i_L(t) \mathrm{d}t$$
$$= \frac{NV_1V_2T_{hc}(8d-9d^2+16D-24Dd-16D^2)}{4(2-d)L} \quad (15)$$

Refined the optimal phase-shift ratio $D^*[n+1]$ employing EMPC is given by,

$$D^*[n+1] = D[n] + d^* = \frac{(4-3D[n])K_1+2K_2}{9K_1}$$
$$- \frac{2\sqrt{4(1+3D[n])K_1^2-2(7+6D[n])K_1K_2+K_2^2}}{9K_1} \quad (16)$$

☺ (16) gives a more accurate prediction of the optimal phase-shift ratio for SS-OTPSM, compared to (11).

Selection of Control Parameters

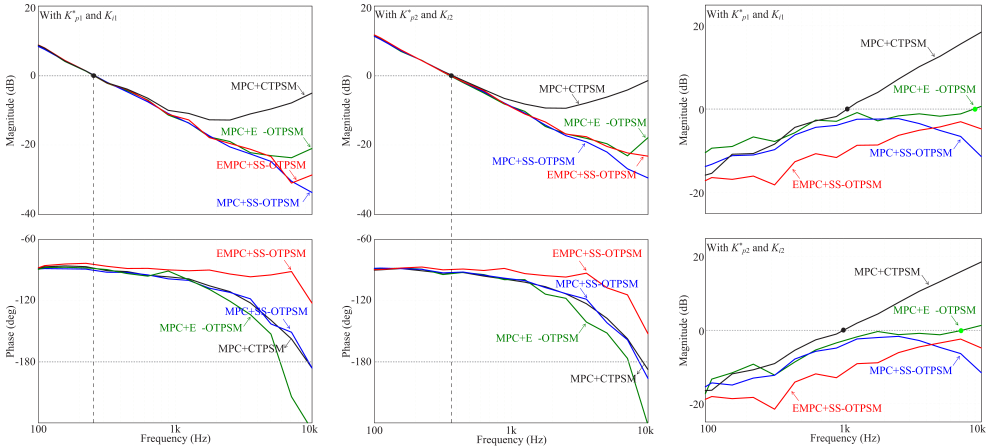

Figure 21: Simulated loop gains and closed-loop output impedances under different systems. (a) Loop gains with $K^*_{p1}=0.07$ and $K_{i1}=0.3$. (b) Loop gains with $K^*_{p2}=0.1$ and $K_{i2}=0.5$. (c) Closed-loop output impedances.

Closed-Loop Simulations of Different MPC Systems

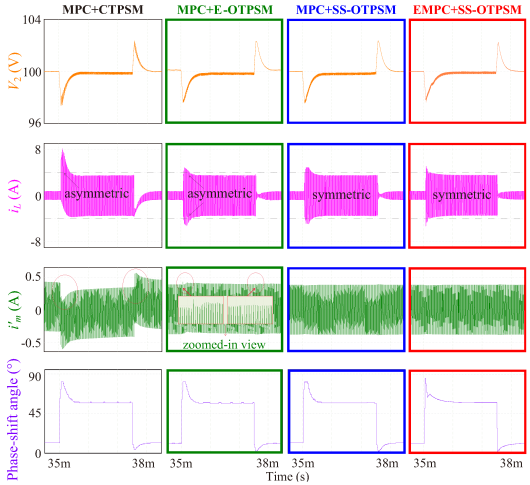

Figure 22: Simulated closed-loop transient responses of different MPC systems for step-load changes between 25% and 95% of the full load with K^*_{p2} and K_{i2}.

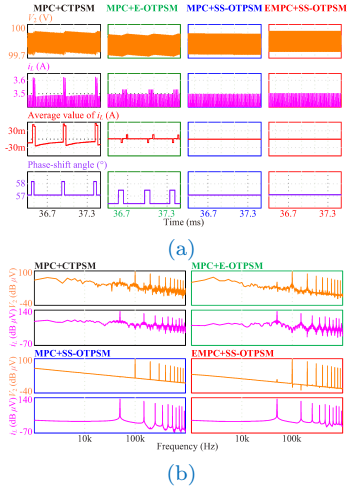

Figure 23: (a) Simulated steady-state waveforms at heavy loads. (b) FFT spectrum analysis.

Closed-Loop Tests #1 Step-Up Load Change

(a) MPC+CTPSM (b) MPC+SS-OTPSM (c) EMPC+SS-OTPSM

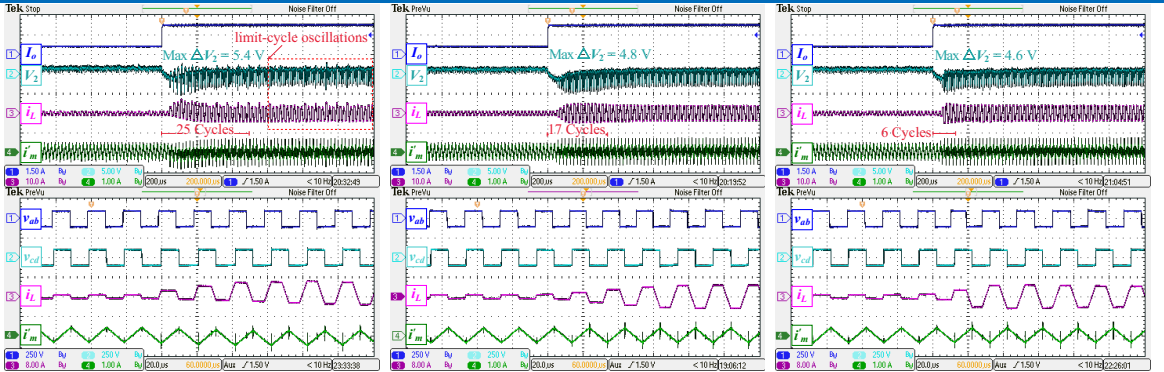

(a) (b) (c)

Figure 24: Experimental closed-loop transient responses for a step change in the load with $\{K^*_{p2}=0.1,\ K_{i2}=0.5\}$.

- ☹ MPC+CTPSM leads to the largest output voltage deviation, longest settling time, and excessive overshoots and transient dc offsets in both i_L and i_m.
- ☺ Under EMPC+SS-OTPSM, the settling times can be significantly reduced to 6-8 cycles with no obvious increase in the overshoot of i_L and i_m, and the output voltage deviation is also the smallest.

Closed-Loop Tests #2 Step-Down Load Change

(a) MPC+CTPSM (b) MPC+SS-OTPSM (c) EMPC+SS-OTPSM

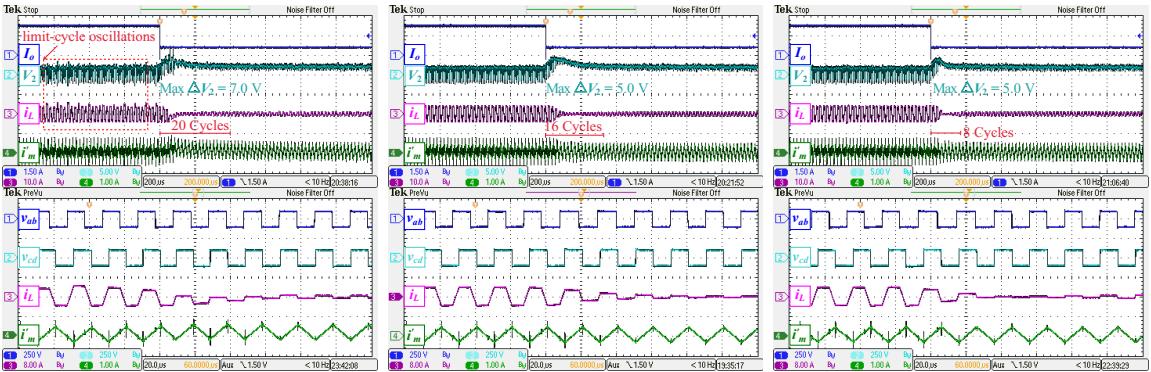

Figure 25: Experimental closed-loop transient responses for a step change in the load with $\{K^*_{p2} = 0.1,\ K_{i2} = 0.5\}$.

- The small-amplitude limit-cycle oscillations in the steady-state waveforms under MPC+CTPSM are caused by the presence of residual transient dc offsets, which can be avoided under MPC+SS-OTPSM and EMPC+SS-OTPSM as SS-OTPSM can achieve complete elimination of all transient dc offsets.

Closed-Loop Tests #3 Performance Evaluation

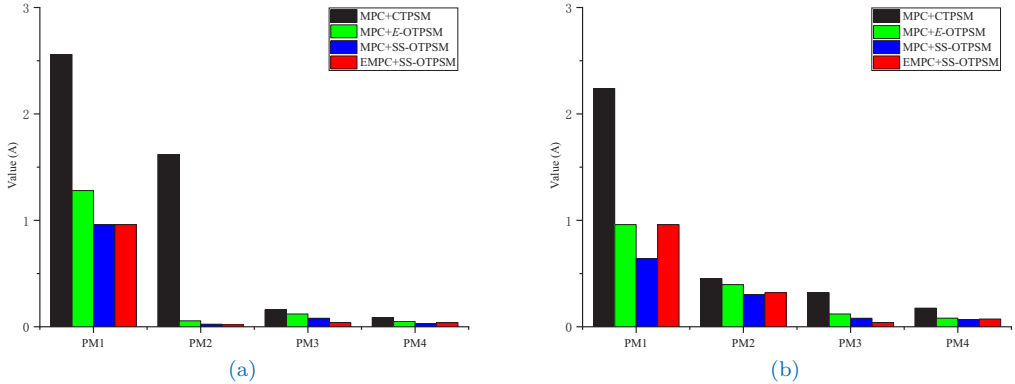

Figure 26: Performance evaluation of closed-loop tests: (a) Load Step-Up Transition. (b) Load Step-Down Transition.

- ☺ MPC+SS-OTPSM outperforms MPC+CTPSM and MPC+E-OTPSM in the four indexes.
- ☺ EMPC+SS-OTPSM enables an optimal performance with fastest dynamics and best waveform quality.

Contents

- Introduction
- Overview of Existing Modulation and Control Strategies
- Optimized Transient Phase-Shift Modulation for NR-DABC
- Optimized Transient Phase-Shift Modulation for SR-DABC
- Conclusions

Steady-State Analysis of SPS-Modulated SR-DABC

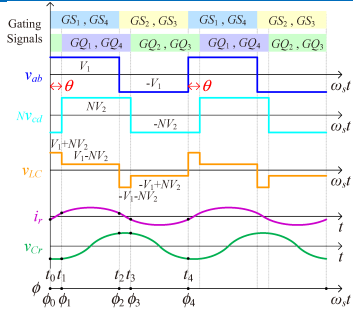

Figure 27: Time-domain waveforms.

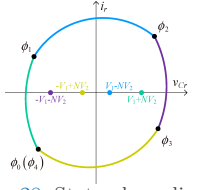

Figure 28: State-plane diagram.

Time-Domain Analysis of Steady-State SPS Modulation

The L_r-C_r tank is excited by a multi-level voltage $v_{LC} = v_{ab} - Nv_{cd}$.

Applying Kirchhoff's voltage law (KVL) and symmetrical characteristics, the analytical expressions of i_r and v_{Cr}:

$$i_r\left(\frac{\phi}{\omega_s}\right)=i_r\left(\frac{\phi_i}{\omega_s}\right)\cos\frac{\phi-\phi_i}{F}+\frac{v_{LC}-v_{Cr}\left(\frac{\phi_i}{\omega_s}\right)}{Z_r}\sin\frac{\phi-\phi_i}{F} \tag{17}$$

$$v_{Cr}\left(\frac{\phi}{\omega_s}\right)=v_{LC}\cdot\left(1-\cos\frac{\phi-\phi_i}{F}\right)+v_{Cr}\left(\frac{\phi_i}{\omega_s}\right)\cos\frac{\phi-\phi_i}{F}+Z_r\cdot i_r\left(\frac{\phi_i}{\omega_s}\right)\sin\frac{\phi-\phi_i}{F} \tag{18}$$

The values of $i_r(\phi_i/\omega_s)$ and $v_{Cr}(\phi_i/\omega_s)$ at different points ϕ_i can be solved exactly. For example,

$$i_r\left(\frac{\phi_0}{\omega_s}\right)=\frac{1}{Z_r}\left[NV_2\sec\left(\frac{\pi}{2F}\right)\sin\left(\frac{\pi-2\theta}{2F}\right)-V_1\tan\left(\frac{\pi}{2F}\right)\right] \tag{19}$$

$$v_{Cr}\left(\frac{\phi_0}{\omega_s}\right)=NV_2\left[1-\cos\left(\frac{\theta}{F}\right)-\sin\left(\frac{\theta}{F}\right)\tan\left(\frac{\pi}{2F}\right)\right] \tag{20}$$

Open-Loop Simulations Under CTPSM in SR-DABC

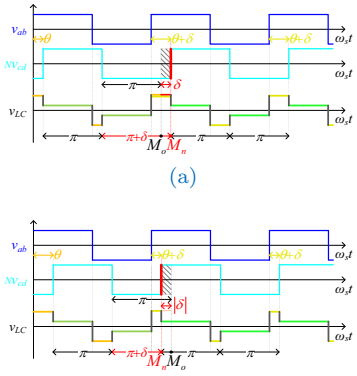

Figure 29: **CTPSM** for (a) $\delta > 0$ and (b) $\delta < 0$.

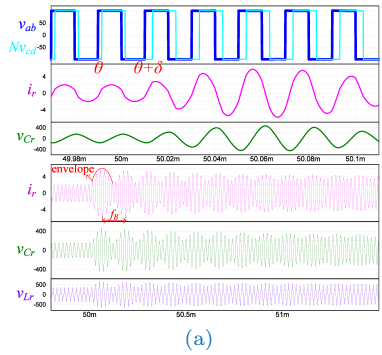

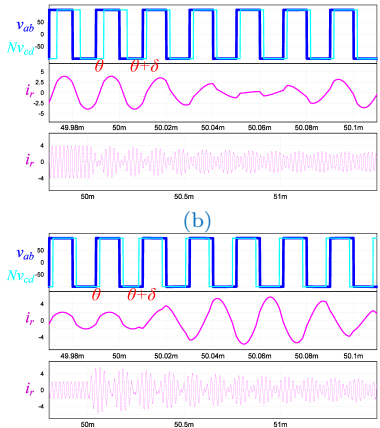

Figure 30: Simulated transient responses under **CTPSM**. (a) Step-load increase: $\theta = \pi/6$, $\delta = \pi/6$ and $\theta+\delta = \pi/3$. (b) Step-load decrease: $\theta = \pi/3$, $\delta = -\pi/6$ and $\theta+\delta = \pi/6$. (c) Step change of power flow direction: $\theta = \pi/6$, $\delta = -\pi/3$ and $\theta+\delta = -\pi/6$.

OTPSM for Transient-Oscillation Elimination

How to effectively modify the transient trajectories of resonant waveforms of SR-DABC?

Unlike the piecewise-linear inductor current in NR-DABC that can directly reach a specific value by linearly adjusting the turn-on and turn-off pulse widths of some power switches, the trajectory of the non-linear resonant current in SR-DABC cannot be easily modified to follow the changes in pulse durations instantaneously due to the inertia of the resonant tank.

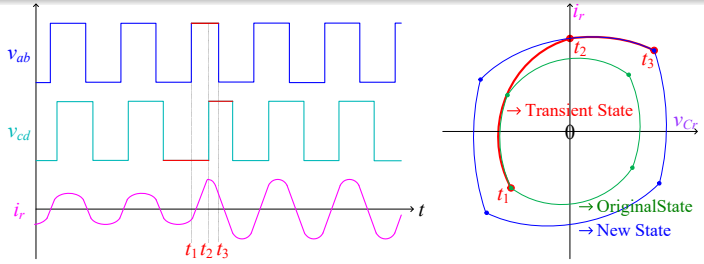

Figure 31: A trajectory-prediction-based OTPSM strategy for SR-DABC (Ref.: ECCE.2018.8558070).

Drawbacks: (1) Closed-form analytical expressions are not available for this OTPSM approach. (2) It requires rich feedback information and high-bandwidth sensors for trajectory planning and computation.

Principles of OTPSM for SPS-Modulated SR-DABC

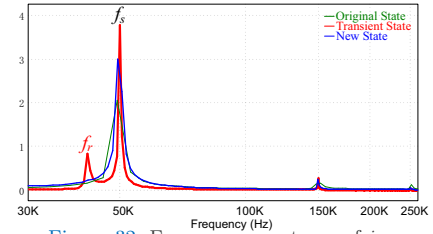

Figure 32: Frequency spectrum of i_r.

☆ Transient oscillations occur at the **beat frequency**: $f_B = f_s - f_r$.

Boundary Constrain Conditions

Assuming the transient process begins at $\phi_4^{\mathrm{I}}/\omega_s$ and ends at $\phi_8^{\mathrm{I}}/\omega_s$.

$$i_r\left(\frac{\phi_8^{\mathrm{I}}}{\omega_s}\right) = i_r\left(\frac{\phi_{12}^{\mathrm{I}}}{\omega_s}\right) \tag{21}$$

$$v_{Cr}\left(\frac{\phi_8^{\mathrm{I}}}{\omega_s}\right) = v_{Cr}\left(\frac{\phi_{12}^{\mathrm{I}}}{\omega_s}\right) \tag{22}$$

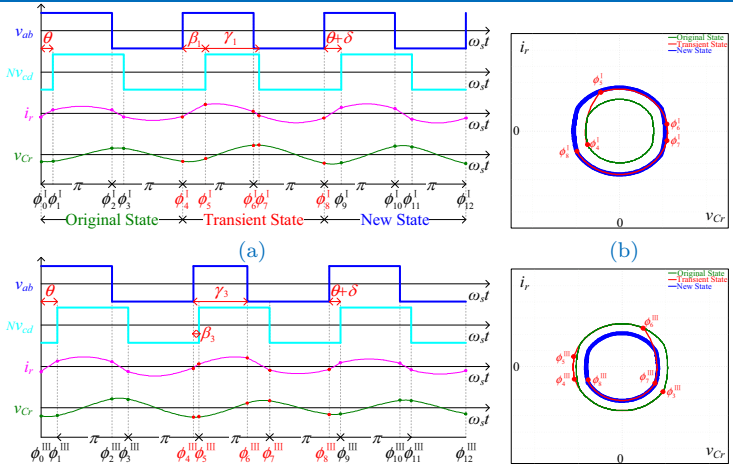

Figure 33: Principles of proposed OTPSM for (a) $\delta > 0$ and (c) $\delta < 0$. 2D state-plane diagrams under OTPSM when (b) $\delta > 0$ and (d) $\delta < 0$.

Open-Loop Simulations Under OTPSM in SR-DABC

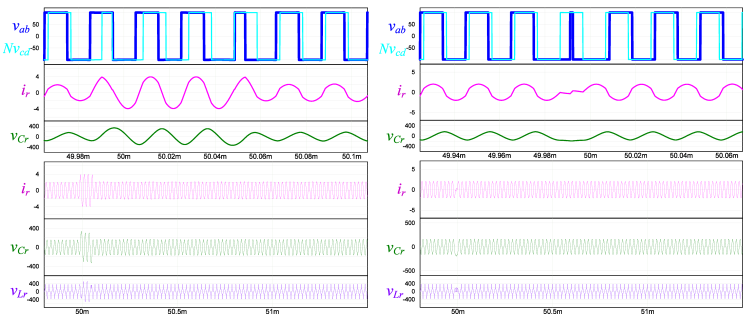

Figure 34: Simulated open-loop transient responses under OTPSM. (a) The phase-shift angle is changed from $\pi/6$ to $\pi/3$ and back to $\pi/6$. (b) The phase-shift angle is changed from $\pi/6$ to $-\pi/6$.

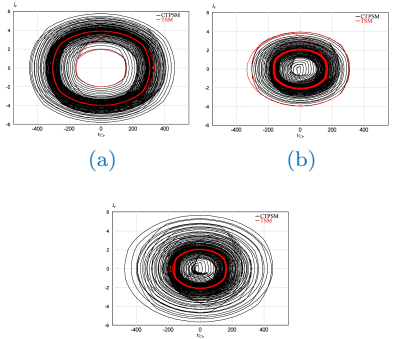

Figure 35: Transient open-loop state-plane diagrams of SR-DABC under CTPSM and OTPSM. (a) $\theta = \pi/6$, $\delta = \pi/6$ and $\theta + \delta = \pi/3$. (b) $\theta = \pi/3$, $\delta = -\pi/6$ and $\theta + \delta = \pi/6$. (c) $\theta = \pi/6$, $\delta = -\pi/3$ and $\theta + \delta = -\pi/6$.

- ☺ No transient oscillations in different open-loop conditions.

Open-Loop Experiments CTPSM v.s. OTPSM

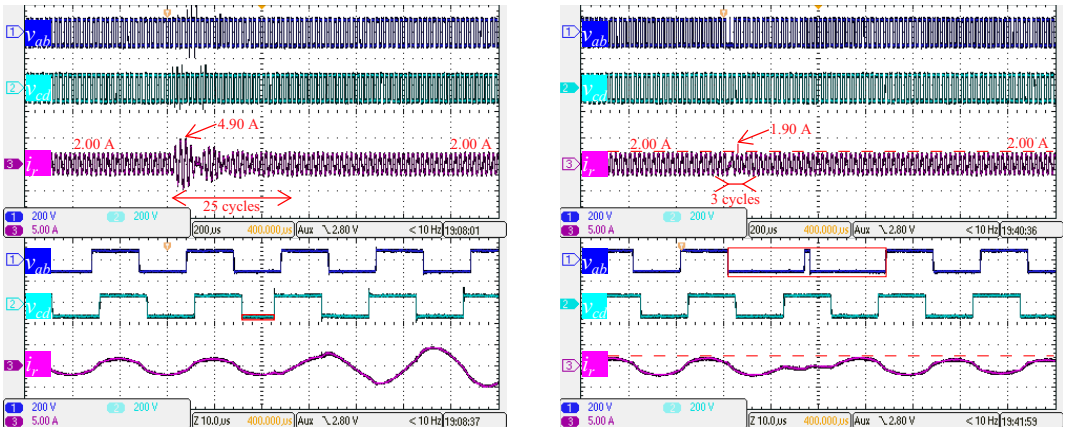

(a) (b)

Figure 36: Open-loop experimental results when the phase-shift angle is changed from $\pi/6$ to $-\pi/6$. (a) Under CTPSM (c.f. simulation results in Fig. 30(c)). (b) Under OTPSM (c.f. simulation results in Fig. 34(b)).

- ☺ OTPSM can eliminate transient oscillations in different open-loop conditions.

MPC Design for SPS-Modulated SR-DABC

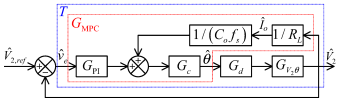

(a)

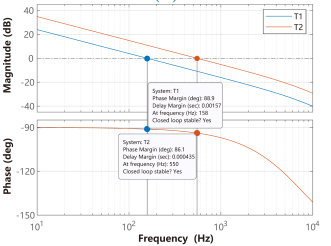

(b)

Figure 37: (a) Small-signal block diagram. (b) Bode plot of loop gain $T(s)$.

Key Design Procedures

① (23) describes the dynamic behavior of V_2:

$$C_o\frac{\mathrm{d}V_2}{\mathrm{d}t}=\bar{i}_2-I_o=\frac{P}{V_2}-I_o=\frac{8NV_1\sin\theta}{\pi^2X_r}-\frac{V_2}{R_L} \tag{23}$$

② Discretizing (23) by using forward Euler approximation yields (24),

$$V_2[n+1]=V_2[n]+V_2'[n]T_s=V_2[n]+\frac{8NV_1\sin\theta}{\pi^2X_rC_of_s}-\frac{V_2[n]}{R_LC_of_s} \tag{24}$$

③ The cost function J is formulated as $J=[V_{2,ref}-V_2[n+1]]^2$.

④ Minimizing J $(\nabla J=0)$ gives the optimal phase-shift angle:

$$\theta[n+1]=\arcsin\left[\frac{\pi^2X_rC_of_s}{8NV_1[n]}\left[v_e[n]+\frac{I_o[n]}{C_of_s}\right]\right] \tag{25}$$

⑤ A PI compensator is introduced to compensate for unmodeled effects and act as a low-pass filter for attenuating HF noise and ensuring loop stability. The overall transfer function is given by:

$$G_{\mathrm{MPC}}(s)=W\left[\hat{v}_e[n]\left(K_p+\frac{K_i}{s}\right)+\frac{\hat{I}_{RL}[n]}{C_of_s}\right]\Big/\sqrt{1-\left[\frac{WI_o[n]}{C_of_s}\right]^2} \tag{26}$$

Closed-Loop Simulation Results with MPC #1

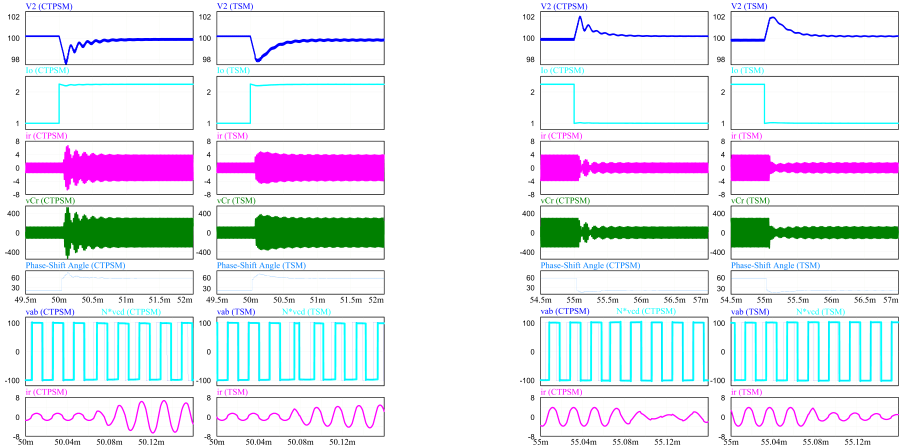

Figure 38: Simulated transient responses under MPC with T_2 ($K_p = 0.07$, $K_i = 0.01$). (a) Load step-up. (b) Load step-down.

- ☺ OTPSM is effective to eliminate the transient oscillations with different control parameters.

Closed-Loop Simulation Results with MPC #2

(modified R_L)

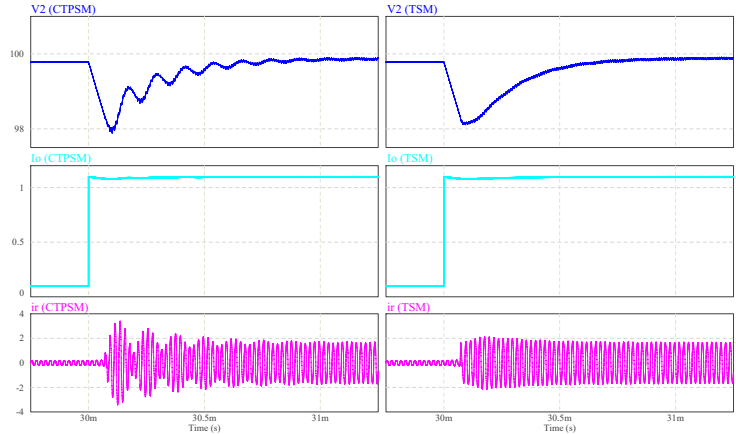

(a)

- ☺ TSM is effective to eliminate the transient oscillations with different amplitudes of load change.

Closed-Loop Simulation Results with MPC #3

(modified R_L, C_o, f_s, K_p, and K_i)

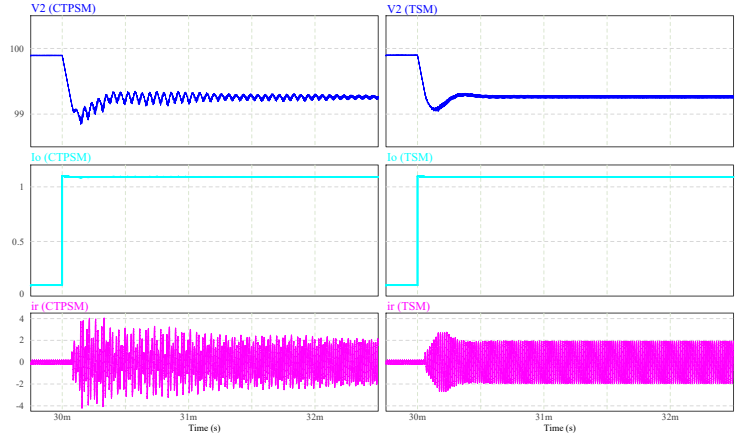

(b)

Figure 39: Simulated closed-loop transient responses under MPC with modified parameters. (a) $C_o = 47\mu$F, $R_L = 1000/90.9\Omega$, $f_s = 50$ kHz, $K_p = 0.07$, and $K_i = 0.01$ (i.e., T_2). (b) $C_o = 100\mu$F, $R_L = 1000/90.9\Omega$, $f_s = 60$ kHz, $K_p = 0.3$, and $K_i = 0.9$.

■ ☺ OTPSM is still effective to eliminate the transient oscillations with different system parameters.

Closed-Loop Experiments MPC+CTPSM v.s. MPC+OTPSM

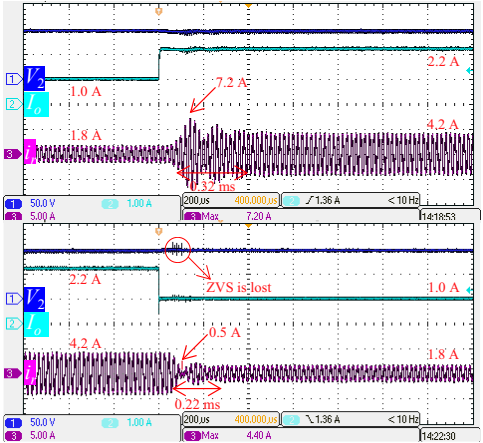

(a)

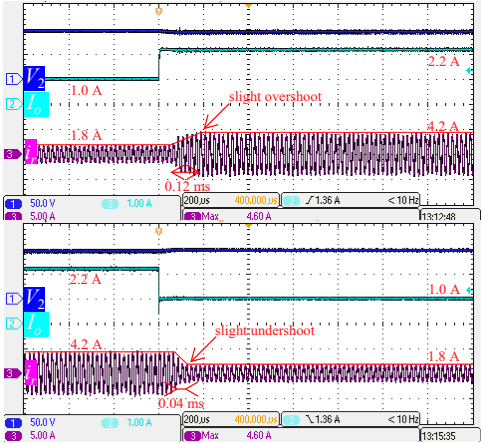

(b)

- ☺ No visible overshoot and undershoot are observed in i_r during step-load increase and decrease when OTPSM is applied instead of CTPSM, and OTPSM can achieve high-quality transient waveforms.

Closed-Loop Experiments MPC+CTPSM v.s. MPC+OTPSM

(zoomed-in waveforms of v_{ab}, v_{cd}, and i_r)

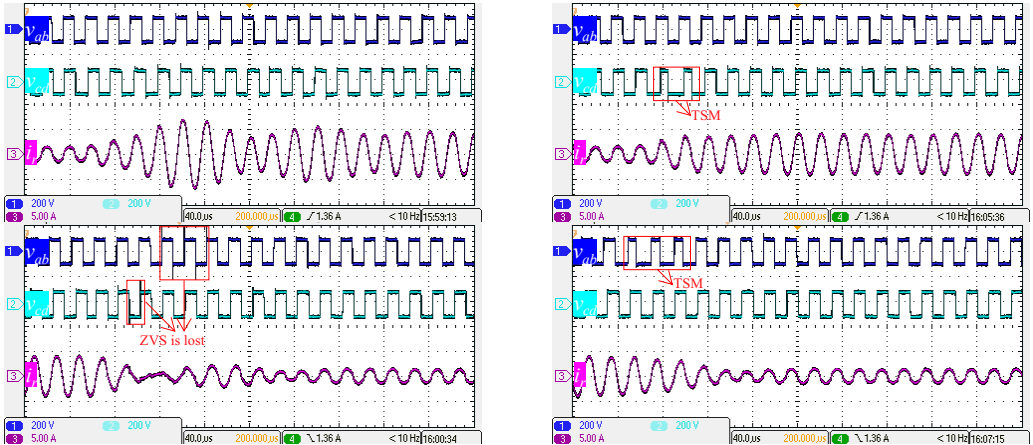

Figure 40: Experimental step-load transient responses under (a) MPC+CTPSM, (b) MPC+OTPSM. Zoomed-in waveforms of v_{ab}, v_{cd}, and i_r under (c) MPC+CTPSM, (d) MPC+OTPSM. (T_2: $K_p = 0.07$, $K_i = 0.01$)

Equivalent Circuit Model of TPS-modulated SR-DABC

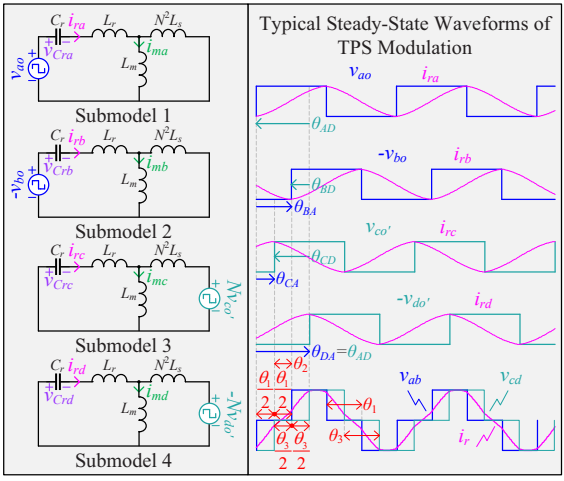

Figure 41: Half-bridge equivalent model.

v_{ab} and v_{cd} under any commonly used fixed-frequency phase-shift modulation schemes can be seen as produced by four independent half-bridge square-wave generators (i.e., v_{ao}, $-v_{bo}$, $v_{co'}$, and $-v_{do'}$).

Contribution of Each Excitation Source

Using the superposition theorem yields

$$\begin{cases} i_r = i_{ra} + i_{rb} + i_{rc} + i_{rd} \\ i_m = i_{ma} + i_{mb} + i_{mc} + i_{md} \\ v_{Cr} = v_{Cra} + v_{Crb} + v_{Crc} + v_{Crd} \end{cases} \tag{27}$$

Applying mesh analysis to submodels 2 and 3

$$i_{mb} = \frac{N^2 L_s}{L_m + N^2 L_s} i_{rb} \tag{28}$$

$$i_{mc} = \left(\frac{1}{\omega_s^2 L_m C_r} - \frac{L_r}{L_m}\right) i_{rc} \tag{29}$$

Open-Loop Simulation Example under CTPSM

from SPS Mode to TPS Mode

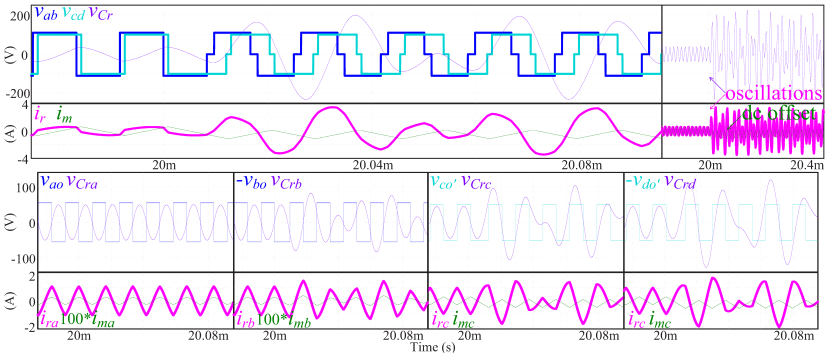

(a)

CTPSM

During transient state, the low-level durations of $-v_{bo}$, $v_{co'}$, and $-v_{do'}$ are directly increased/decreased by $\Delta\theta_{BA}$, $\Delta\theta_{CA}$, and $\Delta\theta_{DA}$, respectively, with respect to v_{ao}.

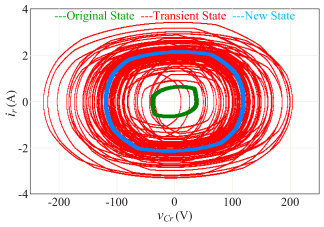

(b)

Figure 42: An open-loop simulation example under CTPSM with $V_1 = 110$ V, $V_2 = 100$ V, $f_s = 60$ kHz, and $F = 1.54$. In this simulation test, the scenario $\theta_1 = 0$, $\theta_2 = \pi/9$, $\theta_3 = 0$, $\Delta\theta_1 = \pi/6$, $\Delta\theta_2 = 11\pi/36$, and $\Delta\theta_3 = \pi/9$, i.e., a transition from SPS mode to TPS mode is simulated. (a) Simulated transient waveforms. (b) v_{Cr}-i_r state-plane diagram under CTPSM.

- ☹ Obvious transient oscillations and dc offset can be observed under CTPSM.

Principles of OTPSM for TPS-Modulated SR-DABC

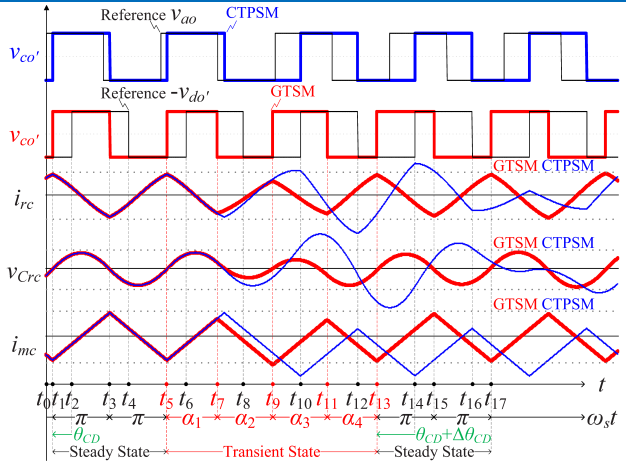

(a)

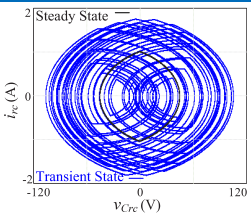

(b)

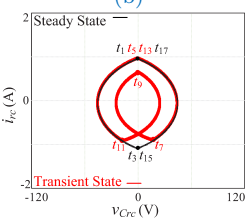

(c)

Figure 43: (a) Theoretical transient waveforms with CTPSM and the proposed OTPSM in submodel 3. (b) v_{Crc}-i_{rc} state-plane diagram under CTPSM. (c) v_{Crc}-i_{rc} state-plane diagram under OTPSM.

Boundary Conditions

for Realizing DC-Offset-Free Transient Response

Elimination of Transient DC Offset

According to (28), any operation in i_{mc} and/or i_{md} may result in large transient dc offsets. It is suggested that $-v_{do'}$ is fixed and used as the reference signal.

The constraint for achieving dynamic volt-second balance during transient state

$$Nv_{co'}\alpha_1 - Nv_{co'}\alpha_2 + Nv_{co'}\alpha_3 - Nv_{co'}\alpha_4 = 0 \quad \Rightarrow \quad \alpha_1 - \alpha_2 + \alpha_3 - \alpha_4 = 0 \tag{30}$$

Phase-shift constraint (to ensure that the transient state ends no later than t_{13})

$$\omega_s(t_{13} - t_5) = \alpha_1 + \alpha_2 + \alpha_3 + \alpha_4 = 4\pi - \Delta\theta_{CD} \tag{31}$$

Combining (30) and (31) leads to

$$\alpha_1 + \alpha_3 = \alpha_2 + \alpha_4 = 2\pi - 0.5\Delta\theta_{CD} \tag{32}$$

To minimize the adverse effects caused by transient dc offset, it is important to minimize the time-averaged value of i_{mc} (i.e., $\bar{i_{mc}}$) over the transient state.

$$\bar{i_{mc}} = \frac{1}{t_{13} - t_5}\int_{t_5}^{t_{13}} i_{mc}\mathrm{d}t = \frac{NV_2}{2L_m}\left(-\frac{T_s}{4} + \frac{2\pi - 0.5\Delta\theta_{CD}}{2} - \frac{\alpha_2\alpha_3}{2\pi - 0.5\Delta\theta_{CD}}\right) \tag{33}$$

For a given $\Delta\theta_{CD}$, $\bar{i_{mc}}$ reaches its minimum value only when (34) holds

$$\alpha_2 = \alpha_3 = \max(\alpha_2) = \max(\alpha_3) \tag{34}$$

Boundary Conditions

for Realizing Oscillation-Free Transient Response

Elimination of Transient Oscillations

i_{rc} and v_{Crc} can be expressed by (35) and (36), respectively,

$$i_{rc}(t) = i_{rc}(t_i)\cos(\omega_r(t-t_i)) + ((-Nv_{co'}) - v_{Crc}(t_i))\sin(\omega_r(t-t_i))/Z_r \tag{35}$$

$$v_{Crc}(t) = v_{Crc}(t_i)\cos(\omega_r(t-t_i)) + Z_r i_{rc}(t_i)\sin(\omega_r(t-t_i)) + (-Nv_{co'})(1-\cos(\omega_r(t-t_i))) \tag{36}$$

The sufficient and necessary condition for effectively suppressing the transient oscillations in i_{rc} and v_{Crc} is that their new steady-state values at t_{13} should be equal to their initial steady-state values at t_5.

$$i_{rc}(t_{13}) = i_{rc}(t_5) \quad \&\& \quad v_{Crc}(t_{13}) = v_{Crc}(t_5) \tag{37}$$

A 4-DOF general solution for the suppression of transient oscillations in i_{rc} and v_{Crc}:

$$2\cos[\frac{\alpha_3+\alpha_4-\alpha_1}{2F}]\sin[\frac{\alpha_2}{2F}] = \sin[\frac{2\pi-0.5\Delta\theta_{CD}-\alpha_4}{F}] \tag{38}$$

☺ GTSM — Optimal 4-DOF Transient Phase-Shift Modulation

To achieve oscillation-free and dc-offset-free dynamics should simultaneously satisfy (32) and (38). Through a careful analysis, only one particular solution set, i.e., the proposed GTSM (39) is available.

$$\begin{cases} \alpha_1 = \alpha_4 = 2\pi - 0.5\Delta\theta_{CD} - \alpha_2 \\ \alpha_2 = \alpha_3 = F\arccos[(1+\cos[\frac{3\pi-\Delta\theta_{CD}}{2F}]\sec[\frac{\pi}{2F}])/2] \end{cases} \tag{39}$$

Open-Loop Simulation Example under OTPSM

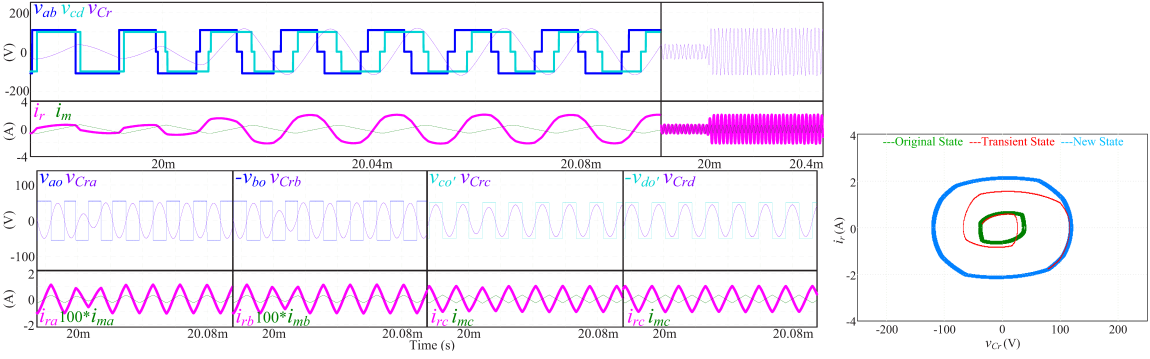

Figure 44: The open-loop simulation examples from SPS mode to TPS mode under OTPSM with $V_1 = 110$ V, $V_2 = 100$ V, $f_s = 60$ kHz, and $F = 1.54$. (a) Simulated transient waveforms under OTPSM. (b) v_{Cr}-i_r state-plane diagrams under OTPSM.

- ☺ OTPSM can achieve a transient performance without overshoot, transient dc offset and oscillations.
- ☺ OTPSM produces lower energy trajectories of i_r and v_{Cr}.

Open-Loop Experiments Under CTPSM v.s. OTPSM

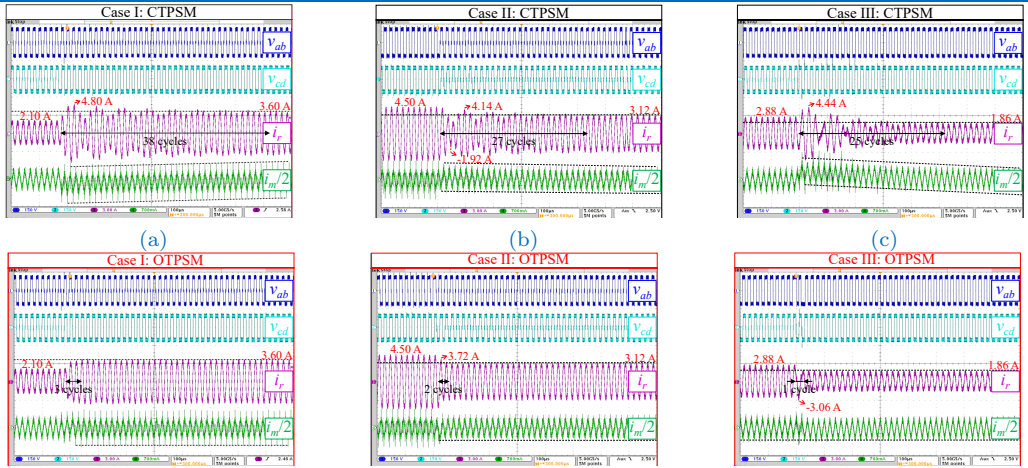

Figure 45: Experimental open-loop transient waveforms with $V_1 = 110$ V, $V_2 = 100$ V, $f_s = 50$ kHz, and $F = 1.2835$. (a) and (d) Case I: Increasing power. (b) and (e) Case II: Decreasing power. (c) and (f) Case III: Reversing power flow direction.

Minimum-RMS-Current Operation for SR-DABC

Minimizing i_{r_RMS}

To maintain a high efficiency during steady state, i_{r_RMS} should be minimized for reducing conduction loss.

$$i_{r\_\mathrm{RMS}} = \sqrt{\frac{1}{T_s}\int_0^{T_s} i_r^2 \mathrm{d}t} = \frac{2\sqrt{2}V_1}{\pi X_r}\sqrt{\begin{array}{l}\cos^2\left[\frac{\theta_1}{2}\right] + M^2\cos^2\left[\frac{\theta_3}{2}\right] \\ -2M\cos\left[\frac{\theta_1}{2}\right]\cos\left[\frac{\theta_3}{2}\right]\cos\left[\theta_2\right]\end{array}} \tag{40}$$

$$P_o = \frac{1}{T_s}\int_0^{T_s} v_{ab}\cdot i_r \mathrm{d}t = \frac{8NV_1V_2}{\pi^2 X_r}\sin\left[\theta_2\right]\cos\left[\frac{\theta_1}{2}\right]\cos\left[\frac{\theta_3}{2}\right] \tag{41}$$

The optimal steady-state phase-shift angles can be obtained by solving the constrained minimization problem:

$$\underset{\boldsymbol{\theta_1},\boldsymbol{\theta_2},\boldsymbol{\theta_3}}{\textbf{minimize}}\ \boldsymbol{i_{r\_\mathrm{RMS}}(\theta_1,\theta_2,\theta_3)},\quad \textbf{subject to}\ \boldsymbol{P_o(\theta_1,\theta_2,\theta_3)=P_{o\_d}}\ \ \&\ \ \boldsymbol{|P_{o\_d}|\le P_{o\_max}} \tag{42}$$

The optimal solution sets can be solved by using the method of **Lagrange multipliers**:

- Case 1 ($M>1$ and $|P_{o\_n}|\le\sqrt{1-1/(M^2)}$):

$$\theta_1 = 0, \theta_2 = \arctan\left[P_{o\_n}\cdot M\right], \theta_3 = 2\arccos\left[\sqrt{1/(M^2)+P_{o\_n}^2}\right] \tag{43}$$

- Case 2 ($M<1$ and $|P_{o\_n}|\le\sqrt{1-M^2}$):

$$\theta_1 = 2\arccos\left[\sqrt{M^2+P_{o\_n}^2}\right], \theta_2 = \arctan\left[P_{o\_n}/M\right], \theta_3 = 0 \tag{44}$$

- Case 3 (other operating regions):

$$\theta_1 = 0, \theta_2 = \arcsin\left[P_{o\_n}\right], \theta_3 = 0 \tag{45}$$

MPC Design for TPS-Modulated SR-DABC

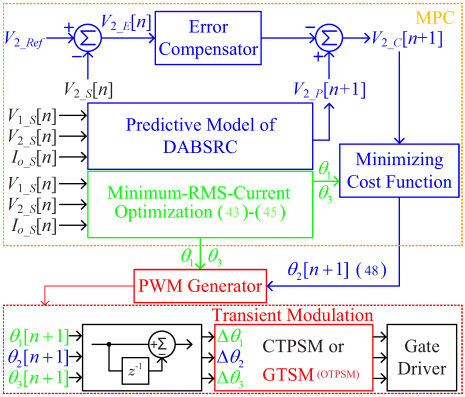

Figure 46: Block diagram of MPC with minimum-RMS-current optimization.

Control Scheme for TPS-Modulated SR-DABC

The dynamics of V_2 can be obtained as

$$C_o\frac{\mathrm{d}V_2}{\mathrm{d}t}=\frac{P_o}{V_2}-I_o=\frac{8NV_1}{\pi^2X_r}\sin[\theta_2]\cos\left[\frac{\theta_1}{2}\right]\cos\left[\frac{\theta_3}{2}\right]-I_o \tag{46}$$

Discretizing (46) using the forward Euler method

$$V_{2\_P}[n+1]=V_{2\_S}[n]+\frac{\mathrm{d}V_{2\_S}[n]}{\mathrm{d}t}T_s \tag{47}$$

Minimizing $\mathcal{J}=(V_{2\_Ref}-V_{2\_C}[n+1])^2$, i.e., $\bigtriangledown\mathcal{J}=0$, yields the predicted optimal outer phase-shift angle

$$\theta_2[n+1]=\arcsin\left[\frac{\pi^2X_rC_of_s}{8NV_{1\_S}[n]\cos\frac{\theta_1}{2}\cos\frac{\theta_3}{2}}\left[\frac{I_{o\_S}[n]}{C_of_s}+K_p^*V_{2\_E}[n]+K_i\sum_{\tau=0}^{n}V_{2\_E}[\tau]\right]\right] \tag{48}$$

When implementing the control loop, the outer phase-shift angle θ_2 is calculated from (48), while the inner phase-shift angles θ_1 and θ_3 are directly determined using (43)-(45).

Closed-Loop Simulation Results with MPC

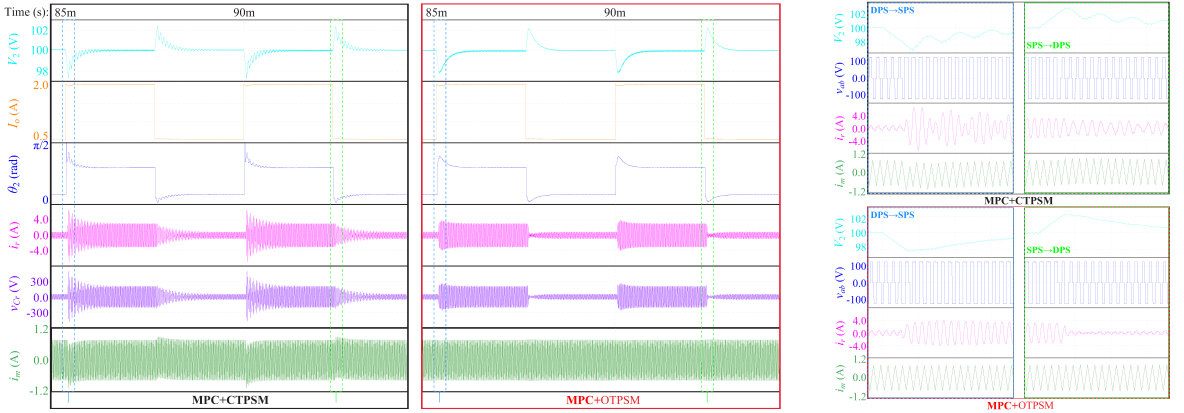

Figure 47: Simulated closed-loop transient waveforms under 200-Hz 0.5-to-2 A pulsed-power loads. $V_1 = 125$ V, $V_2 = 100$ V, $f_s = 50$ kHz, $F = 1.2835$, $K_p^* = 0.08$, and $K_i = 0.00008$.

- ☺ It can be seen that the overshoots and undershoots in i_r, v_{Cr}, and i_m under MPC+CTPSM are significantly larger than those under MPC+OTPSM.

Closed-Loop Tests #1 (a) MPC+CTPSM (b) MPC+OTPSM

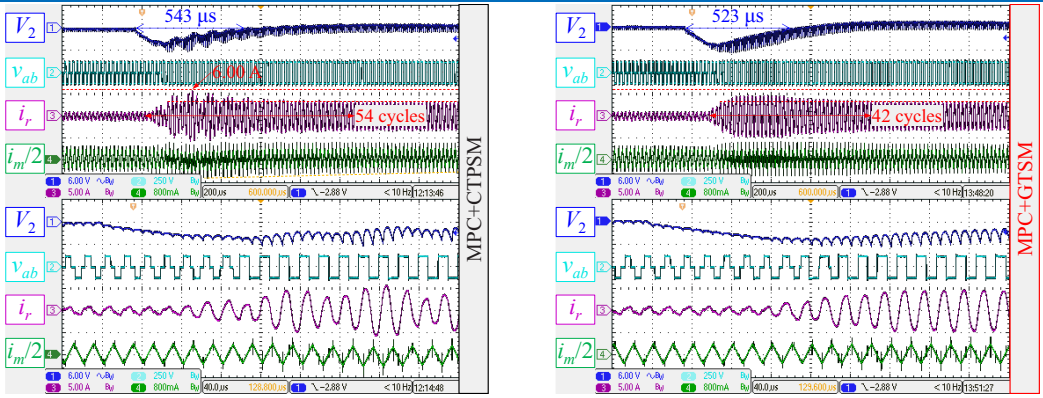

Figure 48: Experimental closed-loop results for a step-up load change from 0.5-2 A with $\{K_p^* = 0.055,\ K_i = 0.0015\}$ under (a) MPC+CTPSM and (b) MPC+OTPSM. $V_1 = 125$ V, $V_2 = 100$ V, $f_s = 50$ kHz, $F = 1.2835$, and $X_r = 39.6317$.

- ☺ The waveforms under MPC+OTPSM can approach their new steady-state values rapidly without undergoing any transient oscillations and dc offsets.

Closed-Loop Tests #2 (a) MPC+CTPSM (b) MPC+OTPSM

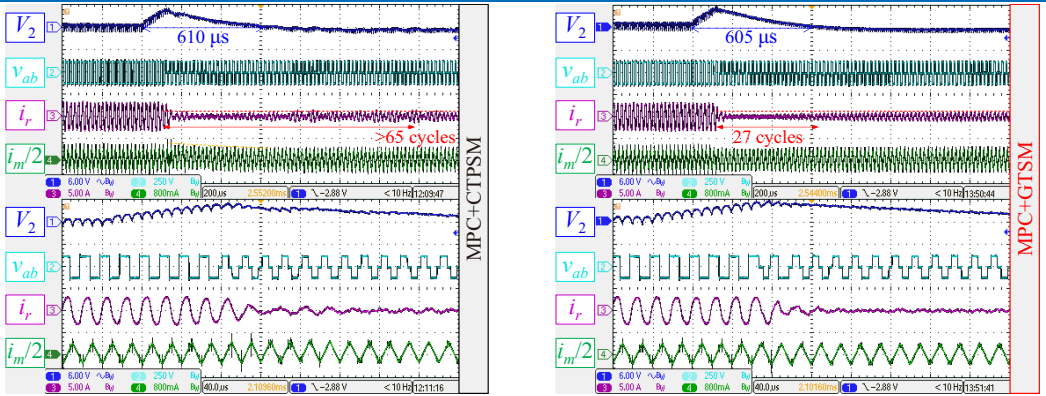

(a) (b)

Figure 49: Experimental closed-loop results for a step-down load change from 2-0.5 A with $\{K_p^* = 0.055,\ K_i = 0.0015\}$ under (a) MPC+CTPSM and (b) MPC+OTPSM. $V_1 = 125$ V, $V_2 = 100$ V, $f_s = 50$ kHz, $F = 1.2835$, and $X_r = 39.6317$.

- ☺ The output voltage quality is much improved under MPC+OTPSM and does not suffer from any transient oscillations.

Closed-Loop Tests #3 (a) MPC+CTPSM (b) MPC+OTPSM

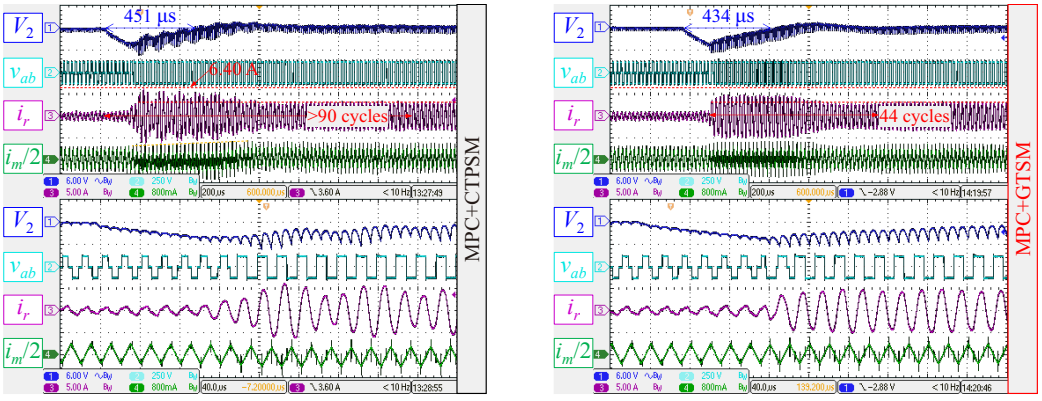

(a) (b)

Figure 50: Experimental closed-loop results for a step-up load change from 0.5 to 2 A with $\{K_p^* = 0.15,\ K_i = 0.004\}$ under (a) MPC+CTPSM and (b) MPC+OTPSM. $V_1 = 125$ V, $V_2 = 100$ V, $f_s = 50$ kHz, $F = 1.2835$, and $X_r = 39.6317$.

- ☺ MPC+OTPSM leads to shorter recovery time in V_2 and shorter settling times in i_r and i_m.

Closed-Loop Tests #4 (a) MPC+CTPSM (b) MPC+OTPSM

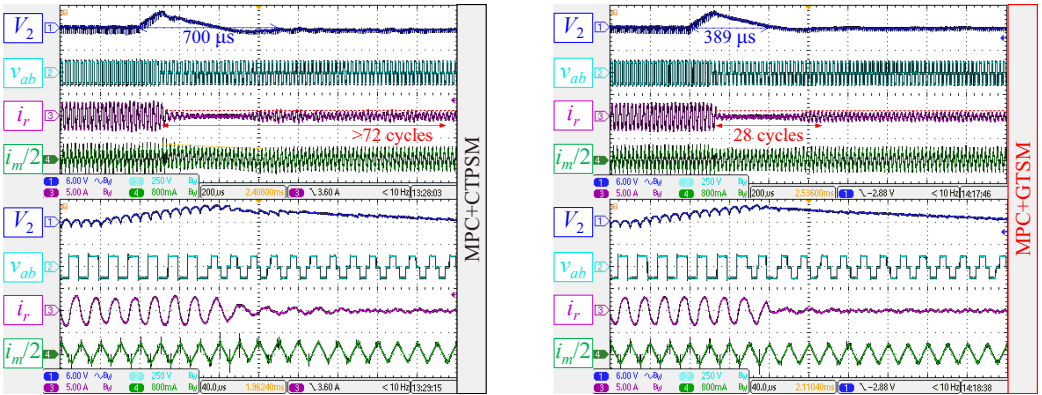

(a) (b)

Figure 51: Experimental closed-loop results for a step-down load change from 2 to 0.5 A with $\{K_p^* = 0.15,\ K_i = 0.004\}$ under (a) MPC+CTPSM and (b) MPC+OTPSM. $V_1 = 125$ V, $V_2 = 100$ V, $f_s = 50$ kHz, $F = 1.2835$, and $X_r = 39.6317$.

When f_r Deviates from Its Nominal Value

☹ Due to aging effects, environmental conditions (e.g., temperature and humidity), manufacturing tolerances, etc., the actual values of C_r and L_r may deviate from their nominal values. From (39) and (48), the algorithms of both OTPSM and MPC are related to $X_r = \omega_s L_r - 1/(\omega_s C_r)$ and $F = f_s/f_r = 2\pi f_s\sqrt{L_r C_r}$, respectively.

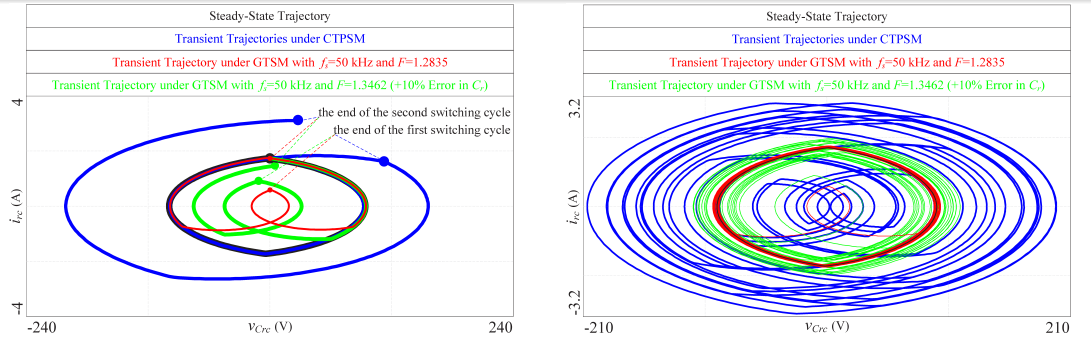

Figure 52: Simulated transient v_{Crc}-i_{rc} state-plane diagrams in submodel 3 under open-loop conditions, where $\Delta\theta_3 = \pi/3$ (i.e., $\Delta\theta_{CD} = \pi/3$), $f_s = 50$ kHz, and $F = 1.2835$ (nominal value) or $F = 1.3462$ (+10% error in C_r). (a) Transient v_{Crc}-i_{rc} state-plane diagrams of the first two switching cycles. (b) Transient v_{Crc}-i_{rc} state-plane diagrams of 25 switching cycles.

Automatic Resonant-Frequency Tracking Technique

A Simple Perturb and Observe (P&O) Method

With large deviations in X_r and F, the performances of both PWM generator and controller can be affected.

According to (41), the estimation of X_r under TPS modulation is given by

$$X_r = \omega_s L_r - 1/(\omega_s C_r) = \frac{8NV_1}{\pi^2 I_o} \sin[\theta_2] \cos\left[\frac{\theta_1}{2}\right] \cos\left[\frac{\theta_3}{2}\right] \tag{49}$$

As X_r changes with f_s (or ω_s) only, f_s must be perturbed to produce different values of X_r.

In theory, for a given switching frequency f_{s_i}, its corresponding impedance X_{r_i} is given by

$$X_{r\_i} = \sqrt{L_r/C_r}\,(F_i - 1/F_i) = Z_r\,(F_i - 1/F_i) \tag{50}$$

Define the nominal impedance X_{r_n} at the nominal switching frequency f_{s_n} as

$$X_{r\_n} = \sqrt{L_r/C_r}\,(F_n - 1/F_n) = Z_r\,(F_n - 1/F_n) \tag{51}$$

Combining (50) and (51), the estimated f_r and F can be obtained from (52) and (53).

$$f_{r\_e} = \sqrt{\frac{X_{r\_ie} f_{s\_i} f_{s\_n}^2 - X_{r\_ne} f_{s\_i}^2 f_{s\_n}}{X_{r\_ie} f_{s\_i} - X_{r\_ne} f_{s\_n}}} \tag{52}$$

$$F_{n\_e} = \sqrt{\frac{f_{s\_n}\,(X_{r\_ie} f_{s\_i} - X_{r\_ne} f_{s\_n})}{f_{s\_i}\,(X_{r\_ie} f_{s\_n} - X_{r\_ne} f_{s\_i})}} \tag{53}$$

Parameter Sensitivity Tests #1 Open-Loop Conditions

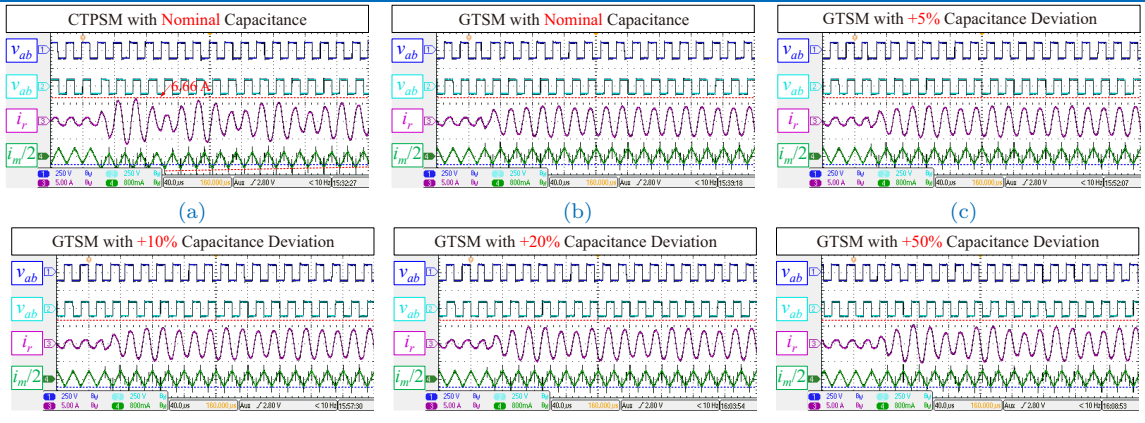

Figure 53: Experimental open-loop transient waveforms under CTPSM and GTSM (OTPSM) while considering different capacitance errors. $V_1 = 110$ V, $V_2 = 100$ V, $f_s = 50$ kHz, $\theta_1 = \Delta\theta_1 = 0$, $\theta_3 = \Delta\theta_3 = 0$, $\theta_2 = \pi/9$, and $\Delta\theta_2 = 4\pi/9$.

- ☺ Even there exists 50% capacitance deviation, OTPSM performs better than CTPSM (smaller transient oscillations in i_r and always no transient dc offset in i_m).

Parameter Sensitivity Tests #2 Closed-Loop Conditions

MPC+CTPSM

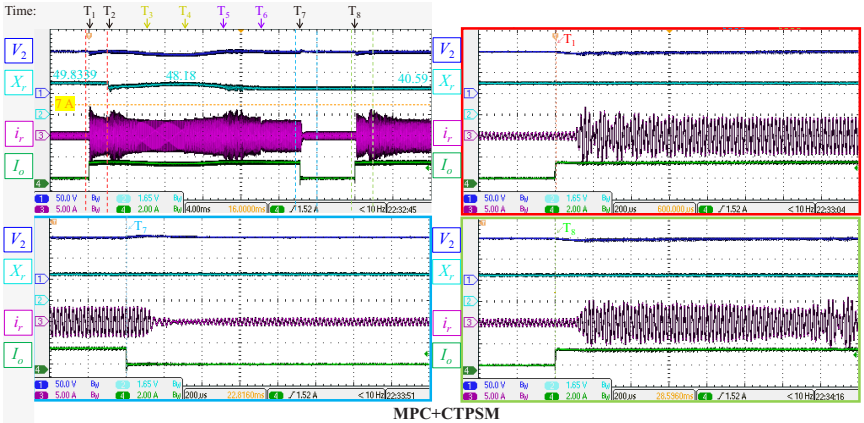

(a)

- The automatic resonant-frequency tracking technique starts from T_2 and will last until T_6.
- ☺ MPC+OTPSM always shows a significantly better transient performance over MPC+CTPSM, as transient oscillations can be observed under MPC+CTPSM.

Parameter Sensitivity Tests #2 Closed-Loop Conditions

MPC+OTPSM

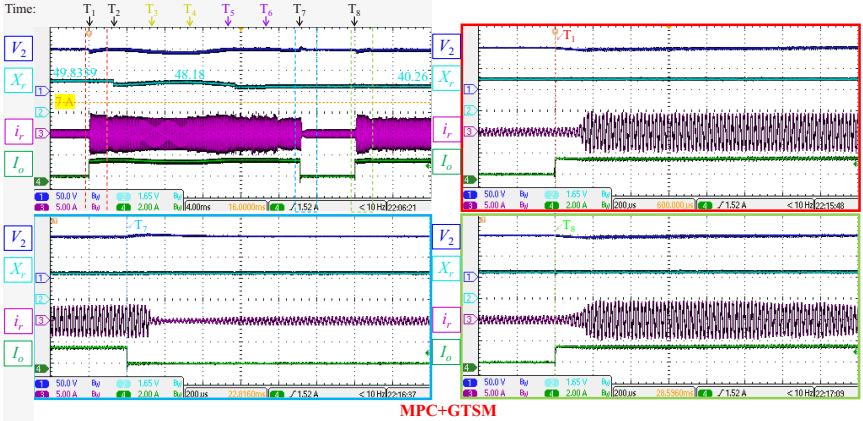

(b)

Figure 54: Experimental closed-loop online estimation of X_r and F. Transient waveforms for step load changes between 0.5 and 2 A are shown under (a) MPC+CTPSM and (b) MPC+OTPSM. $V_1 = 110$ V, $V_2 = 100$ V, $K_p^* = 0.08$, $K_i = 0.002$, $f_{s\_n} = 50$ kHz, $f_{s\_i} = 52$ kHz, initial (incorrect) values of $X_r = 49.8339$ and $F = 1.4060$.

Contents

- Introduction
- Overview of Existing Modulation and Control Strategies
- Optimized Transient Phase-Shift Modulation for NR-DABC
- Optimized Transient Phase-Shift Modulation for SR-DABC
- Conclusions

Key Research Findings and Design Philosophy

Research Findings

1. Implementing OTPSM technology cycle by cycle in a closed-loop DAB system can significantly reduce transient dc offsets and high-frequency oscillations of the high-frequency-link currents, thereby indirectly increasing the control bandwidth and reducing the burden of controller design.
   牵一发动全身，一子落满盘活
2. OTPSM strategies are more suitable for use in combination with high-gain and fast controllers.
   好马配好鞍
3. The deep integration and co-optimization of the Controller and Actuator (PWM Generator) can achieve truly optimal dynamic performance.
   调控相融，珠联璧合，相得益彰

Design Philosophy of OTPSM

1. **Versatility**: OTPSM should preferably be compatible with different steady-state modulation strategies.
2. **Simplicity**: OTPSM should preferably be easily implemented on a cycle-by-cycle manner.
3. **Robustness**: OTPSM should preferably be insensitive to changes in circuit and control parameters.

Acknowledgement & Publications

Acknowledgement

I would like to extend my sincere gratitude to my PhD supervisor, Prof. Ka-Hong LOO of The Hong Kong Polytechnic University (PolyU), for his insightful guidance and support during the course of this research.

List of Publications Relevant to This Presentation

C. Sun, X. Jiang, J. Liu, L. Cao, Y. Yang, and K. H. Loo, "A unified design approach of optimal transient single-phase-shift modulation for nonresonant dual-active-bridge converter with complete transient dc-offset elimination," *IEEE Transactions on Power Electronics*, vol. 37, no. 11, pp. 13 217–13 237, 2022.

C. Sun, X. Jiang, L. Cao, and K. H. Loo, "Total suppression of high-frequency transient oscillations in dual-active-bridge series-resonant converter by trajectory-switching modulation," *IEEE Transactions on Power Electronics*, vol. 37, no. 6, pp. 6511–6529, 2022.

C. Sun, J. Liu, X. Jiang, L. Cao, Y.-C. Wang, J.-X. Shen, and K.-H. Loo, "Generalized multiphase-shift transient modulation for dual-active-bridge series-resonant converter," *IEEE Transactions on Power Electronics*, vol. 38, no. 7, pp. 8291–8309, 2023.

澳门科技大学-创新工程学院-电力电子课题组 简介

学科概况

- **大学世界排名：**THE 251-300 (2026), QS 440 (2026), ARWU 401-500 (2025), U.S. News 699 (2025).
- **学科世界排名：**电气与电子工程 (U.S. News 151), 控制科学与工程 (GRAS 51-75), AI (U.S. News 88)。
- **主要研究方向：**电力电子技术、智能电网的优化调度与运行控制、AI在电气与控制工程领域的应用。

李晓东

澳门科技大学创新工程学院助理院长、计算机科学与工程学院教授、澳门电机及电子工程师学会会长。

https://fie.must.edu.mo/id-1444/person/view/id-541.html

课题组公众号

ID: gh_2a521e606e15

孙川

澳门科技大学创新工程学院工程科学系助理教授、IEEE Macau 理事兼青年学者委员会副主席。

https://chuansun-pe.github.io/

招生信息

- 研究生院官网 https://sgs.must.edu.mo/custom-html/prospective.students.html?locale=zh_MO
- 有意攻读博士学位者，请将简历发送至李老师(xdli@must.edu.mo)或孙老师(csun@must.edu.mo)邮箱。

End of Presentation

THANK YOU VERY MUCH
FOR YOUR TIME AND ATTENTION !

Q&A

澳 門 科 技 大 學
MACAU UNIVERSITY OF SCIENCE AND TECHNOLOGY

Dedication to practical studies,
Enhancement of knowledge, Ability and Quality.
意誠格物